Analysis of local extinction of a n-heptane spray flame using large-eddy simulation with tabulated chemistry

J. Benajes[a], J.M. García-Oliver[a], J.M. Pastor[a,*], I. Olmeda[a], A. Both[b], D. Mira[b]

[a] *CMT-Motores Térmicos, Universitat Politècnica de València, Spain*
[b] *Barcelona Supercomputing Center (BSC), Spain*

Abstract

This work is focused on the study of flame stabilization and local extinction of a spray flame in an atmospheric non-swirled test rig referred to as the CORIA Rouen Spray Burner. This burner shows a double reaction front structure, with an outer laminar diffusion flame and an inner wrinkled partially-premixed flame undertaking local extinction. This unsteady phenomenon is investigated here using large-eddy simulations with a tabulated chemistry method based on steady and unsteady diffusion flamelets with heat loss. A validation of the numerical simulations is conducted first for the carrier and dispersed phase and good agreement with the experimental data is found for mean and fluctuating quantities. The present results were able to to predict relevant parameters of the flame like the lift-off length and flame shape. Numerical results evidence some intermittency on the OH concentration with the presence of high values of formaldehyde indicating the existence of localized extinction in the leading edge of the flame. A detailed analysis showed the impact of droplets on the reacting layer and the existence of rich pockets quenching the flame front. Further downstream, it was shown that when the scalar dissipation rate reaches high values near the reaction zone, the flame front becomes thinner and wrinkled until it eventually quenches. The numerical results evidence that the applied tabulated chemistry method is capable of capturing the local extinction and re-ignition events occurring in the inner layer.

1. Introduction

Current and near-future propulsion technologies mainly rely on liquid-fueled combustion systems [8]. Spray combustion plays a major role in the efficiency and pollutant control in those applications, but remains challenging for both experimental diagnostics and numerical simulations [12, 16]. The complexity arises

*Corresponding author

from the strong interaction between spray, turbulence and combustion chemistry. In order to get further understanding on two-phase flow combustion, dedicated experimental facilities are developed to obtain reliable measurement data during burner operation [24]. These canonical flames allow detailed diagnostics and can be used with high-fidelity models to obtain deep understanding on the flame physics. This is the case of the Coria Rouen Spray Burner (CRSB) [41], which is a reference spray-flame for advanced diagnostics and model assessment.

According to combined experimental and numerical diagnostics [38], this burner shows a double reaction front structure, with an inner wrinkled partially-premixed flame and an outer laminar diffusion flame. A hot region is located between those inner and outer reaction zones, where droplet vaporization is enhanced and most of the vapor fuel that feeds the flame is generated, as already found in other spray-flames analysis [18]. The flame stabilization height is then controlled by the available fuel vapor defined by the polydisperse spray distribution [30].

One of the main issues when addressing this case is how to describe the multimode combustion phenomena characterizing different regions of the flame. In [38] a 2-step scheme in LES using flame resolved simulations and neglecting the subgrid scale wrinkling was employed, so the modelling strategy did not include assumptions of the combustion regime inherently. The overall agreement with the experiments was satisfactory, but the lift-off length was underpredicted. Improved lift-off predictions were obtained by Filtered Tabulated Chemistry (F-TACLES) [4] calculations, where a premixed flamelet manifold was built using a 106-species and 1738-reactions detailed mechanism. This method assumes the flame structure is premixed, and the diffusion burning influencing the flame anchoring and the outer flame layer are neglected. The flame lift-off length was correctly recovered, and the agreement with the experiments was satisfactory. In [39] the Conditional Moment Closure (CMC) method was used to describe the flame structure and double-conditioning was used to account for flame propagation in the limit of negligible scalar dissipation rate of mixture fraction. This approach was also able to reproduce the burning rates and the lift-off length. The analysis of the DCMC equation terms indicated that non-premixed burning modes are prominent at the flame base. It was also shown that the spray vaporization term mainly acts in fuel-rich regions, but evaporative cooling may affect the chemical reaction balance. In this regard, flame local extinctions were investigated in [42] by means of high-speed optical diagnostics applied to the CRSB. Different mechanisms of droplet-turbulence-flame interaction and local extinction phenomena were highlighted from those experimental results, but have not been assessed so far in computations of this burner. As indicated

in [12], flame blow-off transient is characterized by an increase of the degree of local extinction, so accurate modelling of these events is critical for combustor stability simulations.

Tabulated chemistry approaches, such as Flamelet Generated Manifold (FGM) [31] or Flamelet / Progress Variable (FPV) [33] models, are appealing due the possibility to include complex chemistry effects at yet affordable computational cost as described by Chatelier et al. [4]. FGM-RANS simulations were applied to the CRSB in [2], where the main flame characteristics are shown to be properly reproduced. In the present study, a similar approach based on non-adiabatic unsteady flamelet tabulation [22] in a LES framework is applied. The analysis has been focused on the model capability to reproduce droplet-flame and turbulence-flame interactions leading to local quenching and re-ignition in the CRSB. Flamelet approaches successfully captured extinction and re-ignition in gaseous flames [14], but additional effects have to be accounted for in spray flames [22]. The interaction between the droplets and the flame is not fully understood, and introduces complexities in the modelling approach. Based on the model predictions, further insight is provided for the mechanism governing those phenomena. The paper is structured as follows: first, the modelling approach for spray and combustion is described. The test case experimental and numerical setups are presented in Section 3. Finally, the results are discussed in Section 4, followed by the main conclusions.

2. Modelling Approach

The modelling approach employed to describe the multiphase flow problem is based on a Eulerian-Lagrangian description of the spray flame. The gas phase is represented by the Eulerian solver, while the disperse phase of the spray is treated with Lagrangian particles. A Lagrangian Particle Tracking (LPT) method is used to describe the particle transport, which is complemented by heating and evaporation models for the droplets. A fuel droplet is represented by a point mass without volume in the gas phase, so interaction between the two phases can be accounted for by the use of source terms using two-way coupling. The gas phase is described by the use of conservation equations for continuity, momentum, enthalpy and the controlling variables of the flamelet method. A detailed description of this approach in the LES framework is provided in the next subsections.

2.1. Liquid phase

The modelling framework utilizes Lagrangian particles to describe the evaporating droplet cloud. This approximation, which is valid for dilute sprays where the volume fraction of the liquid phase is below a given threshold, is employed here [16]. To describe the state of a droplet, a tracking algorithm is used to obtain

the location, velocity, temperature, and particle sizes by solving ordinary differential equations (ODEs). The first two variables are treated with a kinematic model, while the the thermodynamic conditions of the droplet are given from the heat and mass transfer models. The dominant force considered in the kinematic modelling of droplets is the drag and the governing equations describing the particle transport are given by:

$$\frac{d\boldsymbol{x}_p}{dt} = \boldsymbol{u}_p, \tag{1}$$

$$m_p \frac{d\boldsymbol{u}_p}{dt} = m_p \left(\boldsymbol{u}_p - \tilde{\boldsymbol{u}}\right) \frac{3}{4} \frac{C_D Re_p \rho \nu}{\rho_p d_p^2}, \tag{2}$$

where the subscript p refers to particle information, with $\boldsymbol{x}_p$, $\boldsymbol{u}_p$, m_p, ρ_p, d_p and C_D being the particle position, velocity, mass, density, diameter and drag coefficient. The particle Reynolds number Re_p is given by:

$$Re_p = \frac{d_p |\boldsymbol{u}_p - \tilde{\boldsymbol{u}}|}{\nu}. \tag{3}$$

The rest of parameters refer to gas-phase properties, where u is the gas-phase velocity, and ρ and ν are the density and kinematic viscosity of the surrounding gas. The ODE system of location and velocity is solved by a combined Newmark/Newton-Raphson scheme [13]. The drag coefficient C_D is determined based on the Stokes flow around a sphere, considering high order Reynolds number effects with the Schiller-Naumann correction [16].

The heat transfer between the droplet and the surrounding gas is described by assuming infinite conductivity on the liquid [23], where the droplet temperature T_p is given by:

$$m_p \frac{dT_p}{dt} = \frac{\pi d_p \lambda Nu}{c_{p,p}} \left(\tilde{T} - T_p\right) + \frac{L_v}{c_{p,p}} \frac{dm_p}{dt}, \tag{4}$$

where λ and $\tilde{T}$ are the conductivity and temperature of the gas-phase, while $c_{p,p}$ and L_v refer to the particle heat capacity and lower heating value of the fuel respectively.

Droplet evaporation is described by the Spalding mass transfer number B_M and the Sherwood number Sh as:

$$\frac{dm_p}{dt} = -\pi \rho d_p D_f Sh \ln(1 + B_M), \tag{5}$$

where D_f is the fuel diffusivity and the Spalding number B_M can be obtained from the fuel mass fraction at the interface $Y_{f,i}$ and the surrounding $\tilde{Y}_f$:

$$B_M = \frac{Y_{f,i} - \tilde{Y}_f}{1 - Y_{f,i}}. \tag{6}$$

The system of energy and mass ODEs is strongly coupled, and variations in evaporation rates influence droplet surface temperature. An implicit method is used to solve the heat and mass transfer after the particle velocities are updated. The Reynolds number dependence of the heat and mass transfer rates is modelled using the Ranz-Marshall correlation [37] applied on both the Nusselt *Nu* and Sherwood *Sh* numbers. Additional corrections are introduced following Abramzon and Sirignano [1] to account for Stefan flow, and the interaction between Stefan flow and the flow around the droplet. The liquid phase conservation equations, Eqs. (1), (4) and (5) are employed with the gas phase properties evaluated using the "1/3" law, i.e.: the properties are evaluated at a mean state between the droplet surface conditions and the seen gasses [45].

2.2. Gas phase

2.2.1. Governing equations

The equations describing the gas phase correspond to the low-Mach number approximation of the Navier-Stokes equations with the energy equation represented by the total enthalpy. A Favre-filtered description of the governing equations is followed to avoid the modelling of terms including density fluctuations. Favre-filtering of any quantity ϕ is denoted by $\widetilde{\phi}$, while Reynolds-filtering is given by $\overline{\phi}$. The filtered governing equations for LES correspond to the continuity, momentum and enthalpy and read as:

$$\frac{\partial \bar{\rho}}{\partial t} + \boldsymbol{\nabla} \cdot (\bar{\rho}\tilde{\boldsymbol{u}}) = \bar{S}_C, \tag{7}$$

$$\frac{\partial \bar{\rho}\tilde{\boldsymbol{u}}}{\partial t} + \boldsymbol{\nabla} \cdot (\bar{\rho}\tilde{\boldsymbol{u}}\tilde{\boldsymbol{u}}) = -\boldsymbol{\nabla} \cdot \overline{\tau}_M - \boldsymbol{\nabla}\bar{p} + \boldsymbol{\nabla} \cdot (\bar{\mu}\boldsymbol{\nabla}\tilde{\boldsymbol{u}}) + \bar{S}_M, \tag{8}$$

$$\frac{\partial \bar{\rho}\tilde{h}}{\partial t} + \boldsymbol{\nabla} \cdot \left(\bar{\rho}\tilde{\boldsymbol{u}}\tilde{h}\right) = -\boldsymbol{\nabla} \cdot \overline{\tau}_h + \boldsymbol{\nabla} \cdot \left(\bar{\rho}\tilde{D}\boldsymbol{\nabla}\tilde{h}\right) + \bar{S}_H, \tag{9}$$

where standard notation is used for all the quantities with $\bar{\rho}$, $\tilde{\boldsymbol{u}}$, $\tilde{h}$, $\tilde{D}$, $\bar{p}$ and $\bar{\mu}$ represent the density, velocity vector, total enthalpy (sensible and chemical), diffusivity, pressure and dynamic viscosity using filtered quantities. The τ term stands for the unresolved or subgrid terms related to the filtering operation and applies to the unresolved momentum flux $\overline{\tau}_M$ and the unresolved enthalpy flux $\overline{\tau}_h$. The subgrid viscous stress tensor is determined based on the Stokes' assumption and the turbulence contribution is obtained by the use of the Boussinesq approximation [35]. A unity Lewis number assumption has been made to simplify the scalar transport in the governing equations. Heating due to viscous forces is neglected in the enthalpy equation and the unresolved heat flux is modelled using a gradient diffusion approach [27]. The modelling framework is closed by an appropriate expression for the subgrid-scale viscosity. The eddy-viscosity is

obtained from the Vreman [43] model using a constant $c_k = 0.1$. The same single-value constant has been used in previous studies and it is also retained here [3, 25].

The coupling of the disperse phase with the gas phase is performed by the coupling source terms associated to the mass, momentum and energy exchange ($\bar{S}_C$, $\bar{S}_M$, and $\bar{S}_H$) between the droplets and the gas. The closure for these terms is obtained by the integration of Eqs. (1), (4) and (5) [16]. The governing equations describing the thermochemical evolution of the multi-component mixture are given in the next sub-section.

2.2.2. Turbulent combustion model

The modelling approach used to describe the combustion process and thermochemical composition of the flame is presented here.

Flamelet method

This combustor shows different burning characteristics featuring premixed and diffusion modes simultaneously in different regions of the flame, as indicated in section 1. The inner layer is subjected to strong variations in mixture composition and high strain, the outer layer is laminar and dominated by diffusion. In such conditions, the use of 1D counterflow diffusion flamelets is proposed here to describe the global flame behaviour, as the flame front is controlled by the diffusion of reactants and this mechanism plays a key role in the stabilization of the flame, as pointed out by DCMC LES of this flame [39]. Chatellier et al. [4] proposed a premixed flamelet manifold for this burner, but the diffusion burning influencing the flame anchoring and the outer flame layer was neglected with this approach, as diffusion across mixture fraction lines could not be be described by the tabulation of premixed flamelets [15]. In the inner reaction zone, part of the reacting layer has premixed characteristics accompanied by a diffusion-dominated layer subjected to a highly strained flow field. According to the analysis performed by Liñan et al. [19], as the flow approaches extinction conditions the flame structure between diffusion and premixed flamelets become more similar. This similarity has been also used in [17], and supports the selection of strained diffusion flamelets in this region, which are able to describe both the influence of strain on the flame front and the extinction process.

In this study, the flame structure of this spray flame is described by the flamelet method [32]. A scale separation between the flow and the chemistry is assumed, so that the flame structure can be defined by a composition of one-dimensional (1D) flames. In order to account for strain effects on the thermodiffusive behaviour of the reacting layer, laminar diffusion flamelets at different strain rates are tabulated until the extinction point is encountered. An extinguishing flamelet initiated from the last stable instance (extinction point) is used as a natural continuation of this two-dimensional manifold [6], conducting an unsteady

calculation to account the transient development of the thermochemical state. This flamelet solution covers the entire state space from the stable branch to the mixing line, and is used to provide the thermochemical information of the flame during unsteady processes like extinction or re-ignition.

The chemistry for n-heptane is given by the 188-species skeletal mechanism from Lu and Law [20], and the flamelet equations are solved in physical space with the chem1d code [5] using a unity Lewis number approach. A representation of the manifold in mixture fraction space is shown in Fig. 1a.

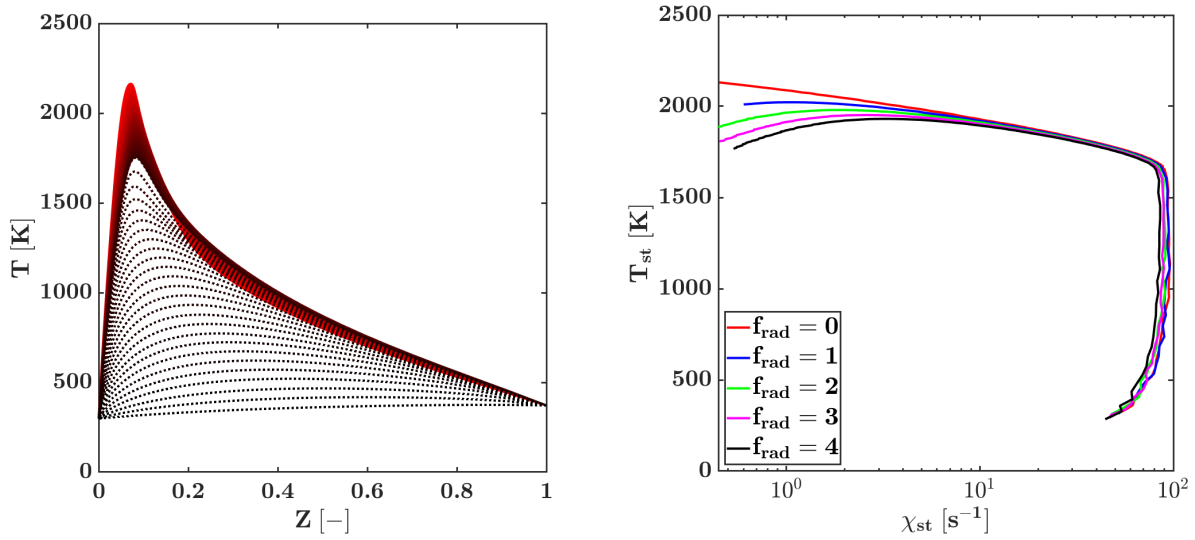

(a) Representation of the flamelet manifold. Solid lines: steady flamelets, dashed lines: extinguishing flamelets. Strain rate represented by colour from red to black as the strain rate increases.

(b) S-curve of the n-heptane flame described by the stoichiometric temperature as function of the strain at different enthalpy levels (described by the scaling of the radiation term f_{rad}).

Figure 1: Flamelets used in the tabulation process.

The effects of heat loss on the flamelet database are considered by the tabulation of strained diffusion flames at different enthalpy levels. In this approach, flamelets always have pure fuel vapour composition prescribed on one inlet, and the local enthalpy deficit is generated through a radiative source term in the energy equation without changing the inlet temperature of the reactants. Thus, only the local heat loss effect is modelled, which allows a relatively simple tabulation process, with only two degrees of freedom: enthalpy level and strain rate.

The enthalpy level of the mixture can be characterised by the scaled enthalpy $\tilde{i}$, which is computed from the transport of total enthalpy $\tilde{h}$, see Eq.(9) on the gas phase model, as:

$$\tilde{i} = \frac{\tilde{h} - h_{min}}{h_{max} - h_{min}}. \tag{10}$$

This enthalpy scaling is defined by the maximum and minimum enthalpy levels, h_{max} and h_{min} given in the low-dimensional manifold for each mixture fraction and reaction progress. Different enthalpy levels are reached by the scaling of the radiative term (f_{rad}).

The effect of the enthalpy on the thermochemical properties of the flame can be distinguished in Fig. 1b. It shows a higher influence of the enthalpy level at low scalar dissipation rates. The effect of heat loss on the extinction is summarised in Tab.1. The extinction point is shifted to lower strains as the heat loss is augmented by the up-scaling of the radiative term, though the impact is minor for the operating conditions of the CRSB burner. The time scale of the extinction event is also provided as: $\tau_{ext} = 1/a_{ext}$, this metric agrees well with the time it takes for the unsteady flamelets to extinguish. It is approximately 0.7 ms for all considered heat-loss levels.

Scaling of radiation term	0	1	2	3	4
a_{ext} [1/s]	1496	1452	1416	1375	1335
$T_{st,ext}$ [K]	1656	1657	1651	1651	1650
τ_{ext} [ms]	0.668	0.689	0.706	0.727	0.749

Table 1: Extinction point with different degrees of heat loss (0 scaling is the adiabatic case), a_{ext}: strain rate at the extinction point, $T_{st,ext}$: temperature at stoichiometric composition at the extinction point, τ_{ext}: time scale of extinction.

The tabulation of flamelets at different enthalpy levels is used to account for the heat loss during droplet evaporation. As the evaporation rates are highly sensitive to small temperature variations of the surrounding gas, the addition of these thermal states into the flamelet manifold is important to ensure correct heat and mass transfer during the phase change. Furthermore, it has already been shown that dealing with enthalpy deficit in flames by radiative heat losses can be used as an alternative to other approaches [9]. Therefore, this is a reasonable option to account for heat transfer to the droplets, as the evaporation process also requires an exchange of enthalpy similarly to the heat loss in flames.

Governing equations

Three controlling variables are used to characterize the thermochemical state of the flamelets composing the manifold: mixture fraction Z, progress variable Y_c, and normalized enthalpy i. The mixture fraction is determined by Bilger's formula, while the progress variable Y_c in our study is defined as:

$$Y_c = \sum_{k=1}^{N} \frac{a_k}{W_k} Y_k, \tag{11}$$

with $N = 4$ using $Y_k = \{Y_{CO_2}, Y_{CO}, Y_{H_2}, Y_{H_2O}\}$, and W_k being the molar weight of the chemical species. The

contribution of each species to the progress variable Y_c is given by the coefficients $a_k = \{4.0, 1.0, 0.5, 2.0\}$ respectively, proposed by Ma [21].

Transport equations for the filtered controlling variables $\tilde{Z}$ and $\tilde{Y}_c$ are defined in order to describe the chemical evolution of the reacting flow, as the normalize enthalpy $\tilde{i}$ is obtained directly from the enthalpy, see Eqs. (9) and (10). The systems of equations read:

$$\frac{\partial \overline{\rho}\tilde{Z}}{\partial t} + \boldsymbol{\nabla} \cdot \left(\overline{\rho}\tilde{\boldsymbol{u}}\tilde{Z}\right) = -\boldsymbol{\nabla} \cdot \overline{\tau}_Z + \boldsymbol{\nabla} \cdot \left(\bar{\rho}\bar{D}\boldsymbol{\nabla}\tilde{Z}\right) + \bar{S}_Z, \tag{12}$$

$$\frac{\partial \overline{\rho}\tilde{Y}_c}{\partial t} + \boldsymbol{\nabla} \cdot \left(\overline{\rho}\tilde{\boldsymbol{u}}\tilde{Y}_c\right) = -\boldsymbol{\nabla} \cdot \overline{\tau}_{Y_c} + \boldsymbol{\nabla} \cdot \left(\bar{\rho}\bar{D}\boldsymbol{\nabla}\tilde{Y}_c\right) + \overline{\dot{\omega}}_{Y_c}. \tag{13}$$

As for the Navier-Stokes equations, Eqs. (7) to (9), the unresolved terms appearing after the LES filtering $\overline{\tau}_Z$ and $\overline{\tau}_{Y_c}$ are closed using a gradient diffusion approach [7]. The source term $\bar{S}_Z$ in the $\tilde{Z}$ equation refers to the mass generated by droplet evaporation, while $\overline{\dot{\omega}}_{Y_c}$ is the filtered progress variable source term.

Turbulent chemistry interaction

In order to account for turbulent/chemistry interactions at the subgrid scale, the tabulated properties ψ from the manifold are integrated with a presumed-shape probability density function (PDF) that describes the statistical effect of turbulence on the flame structure [7]. To facilitate the flamelet manifold tabulation, retrieval and integration, a scaled progress variable C is then defined as:

$$C = \frac{Y_c - Y_{c,min}}{Y_{c,max} - Y_{c,min}} \tag{14}$$

Therefore, this three-dimensional manifold $\psi = \psi(Z, C, i)$ must be integrated with a filtered joint-PDF $\widetilde{P}(Z, C, i)$ as:

$$\widetilde{\psi}(Z, C, i) = \int_0^1 \int_0^1 \int_0^1 \psi(Z, C, i)\widetilde{P}(Z, C, i) dZ dC di. \tag{15}$$

The joint-PDF $\widetilde{P}(Z, C, i)$ of tree independent variables is prohibitively complex for most modelling strategies, thus the joint-PDF is usually treated as a product of statistically independent PDFs of each degree of freedom [14]:

$$\widetilde{P}(Z, C, i) \approx \widetilde{P}_Z(Z)\widetilde{P}_C(C)\widetilde{P}_i(i). \tag{16}$$

In the present non-premixed turbulent combustion model, presumed shape PDFs are employed in each controlling variable. Namely the distribution of mixture fraction is characterised by a β-function uniquely defined by the filtered value $\widetilde{Z}$ and subgrid variance $Z_v = \widetilde{ZZ} - \widetilde{Z}\widetilde{Z}$ of Z. Meanwhile δ-functions are applied to

the scaled progress variable and enthalpy parameter. This modelling strategy assumes, that most unresolved effects are attributed to spatial mixture fraction fluctuations, and the subgrid enthalpy and progress variable variations are a consequence of the varying mixture fraction.

A closure for the subgrid scale variance Z_v is required to recover the tabulated quantities, so a transport equation for Z_v is solved in this study [34] on top of Eqs. (12) and (13). The equation for the mixture fraction subgrid variance is given by:

$$\frac{\partial \overline{\rho} Z_v}{\partial t} + \boldsymbol{\nabla} \cdot (\overline{\rho} \tilde{\boldsymbol{u}} Z_v) = -\boldsymbol{\nabla} \cdot \overline{\tau}_{Z_v} + \boldsymbol{\nabla} \cdot \left(\bar{\rho} \bar{D} \boldsymbol{\nabla} Z_v \right) - 2 \overline{\tau}_Z \cdot \boldsymbol{\nabla} \tilde{Z} - 2 \overline{s}_{\chi Z}, \tag{17}$$

where $\overline{s}_{\chi Z}$ is the unresolved part of the scalar dissipation rate and is modeled assuming a linear relaxation of the variance within the subgrid [7]. Thus $\overline{s}_{\chi Z} = \overline{\rho} \frac{Z_v}{\tau_{SGS}}$, where τ_{SGS} is the sub-grid time scale [3]. The modelling constant of subgrid scalar dissipation of mixture fraction variance is taken as 2, the theoretical value, as shown in Eq.17. The chemical state of the turbulent flame in the LES framework is ultimately described by the four controlling variables: $\widetilde{Z}$, Z_v, $\widetilde{Y_c}$ and $\widetilde{h}$.

The thermochemical table contains then 101x11x101x11 entries corresponding those four controlling variables. For the progress variable discretization, a uniform spacing is used across the flame front, while the mixture fraction space is discretized with a non-uniform distribution centered at the stoichiometric mixture fraction with a growing rate of 1.1 towards the lean and rich sides. The variance of the mixture fraction is discretized with a power function with exponential $p = 3$. The enthalpy level is tabulated for 11 equidistant steps. Note, that the number of these levels is larger than the number of different radiation scalings applied, we chose this approach because the radiation scaling does not guarantee an equidistant spacing in enthalpy, thus more levels are applied in the table to represent the flamelets in sufficient detail.

2.2.3. Numerical methods

The discretization strategy is based on a conservative finite element convective scheme [3], where stabilisation is only introduced for the continuity equation by means of a non-incremental fractional-step method, modified in order to account for variable density flows. The final scheme preserves momentum and angular momentum for variable density flows. The error of kinetic energy conservation is of order O(dt h^{k+1}), thus dissipation is limited. Standard stabilised finite elements are used for the scalars, while the time integration is carried out by means of an explicit third order Runge-Kutta scheme for momentum and scalars. The chosen low dissipation FE scheme presents good accuracy compared to other low dissipation finite volume and finite difference methods with the advantage of being able to increase the order of accuracy at will

without breaking the fundamental symmetry properties of the discrete operators. The proposed modelling and numerical framework has been developed in the multiphysics code Alya [40].

3. Test Case Description

3.1. Experimental setup

The case studied in this work is the n-heptane spray-flame from the CORIA Rouen Spray Burner (CRSB) [41]. The CRSB is an open burner operated with an air mass flow rate of 6 g/s at atmospheric pressure and temperature of 298 K. Air is injected in a plenum and exits to the atmosphere through an annulus-shaped duct with an inner and outer diameter of 10 and 20 mm, respectively, with a Reynolds number ~14000 based on annular jet outlet conditions. The liquid n-heptane injection comes from a hollow-cone pressurized injector (8 bar injection pressure) with a 80º angle and a fuel mass flow rate of 0.28 g/s.

This burner is a reference test case in the Workshop on Turbulent Combustion on Sprays (TCS) [24], with multiple experimental diagnostics available for spray and flame characterization. Droplet size and velocity are measured by Phase Doppler Anemometry (PDA), while gas-phase velocities are obtained by seeding the co-flow [38]. Flame structure is characterized by simultaneous high-speed OH Planar Laser Induced Fluorescence (PLIF) and Particle Image Velocimetry (PIV) measurements. Those techniques allowed the identification of the flame front disruptions due turbulence and droplet interaction [42].

3.2. Numerical setup

The computational domain is based on the experimental test rig described above and presented in Fig. 2 (left). The domain includes a cylindrical volume of 200 mm in radius and 500 mm in height to account for the environment of the flame. The mesh used for this geometry results in a total of 20M elements using a hybrid mesh with tetrahedrons, prisms and pyramids. It is refined to a minimum cell size of 0.2 mm inside the air duct, in the injection region and in the near field of the flame, as shown in Fig. 2 (right). Layers of prisms are applied in the air duct in order to better resolve the boundary layer. Concerning LES quality results, Pope's criterion [36] is used and over 80% of the turbulent kinetic energy is solved in the injection zone and flame base. Further refinement to 79M element mesh was performed in order to check grid convergence, however, it did not exhibit different dynamics or affected significantly the results, so the 20M element mesh was retained for the analysis.

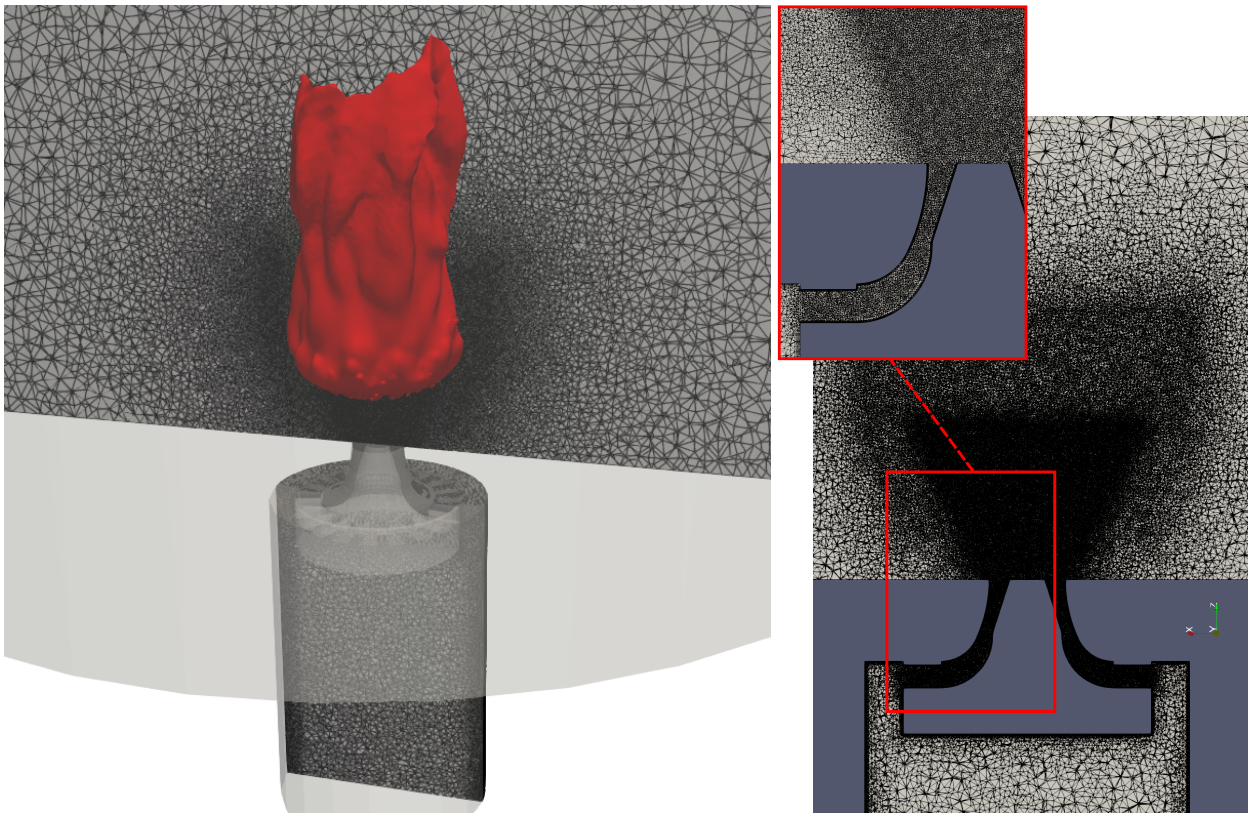

Figure 2: Left: computational domain and overview of the mesh (stoichiometric mixture fraction iso-surface of the flame represented in red colour). Right: detailed view of the mesh in the injection region.

A constant air mass flow rate at 298K is prescribed as inlet condition and non-slip adiabatic walls are used as boundary conditions.

The liquid fuel injection is modeled in a hollow cone shape and droplets are injected in an annulus located 2 mm downstream the nozzle, where it is assumed that the atomization process is completed. A Rosin-Rammler distribution with a Sauter Mean Diameter (SMD, D_{32}) of 32 μm and a q parameter of 2.3 is used to describe the droplet size distribution, given by the experimental data at the closest axial positions. In addition, the initial droplet diameter is limited between 1 μm and 70 μm for numerical feasibility. Droplets are injected with an injection velocity that depends on the size: $v_{inj} = 33$ m/s for droplets with $d < 10$ μm decreasing linearly with diameter to $v_{inj} = 25$ m/s for droplets with $d > 55$ μm, according to [2]. The half injection angle is chosen randomly between 35º and 50º.

In this work, time-averages for both gas phase and droplets statistics are collected over about 100 ms, which correspond to approximately 30 flow-through times. The flow-through is estimated by the averaged axial velocity integrated over a volume enclosing the flame and its surrounding.

4. Results

The following sections include the numerical results of the CRSB using large-eddy simulations. It is divided into different sections: comparison of the flow field and dispersed phase with the experimental measurements, the study of the flame structure, and the analysis of the local extinction events. To compare the results with the experimental data, three radial stations at different axial positions are considered, see Fig. 3.

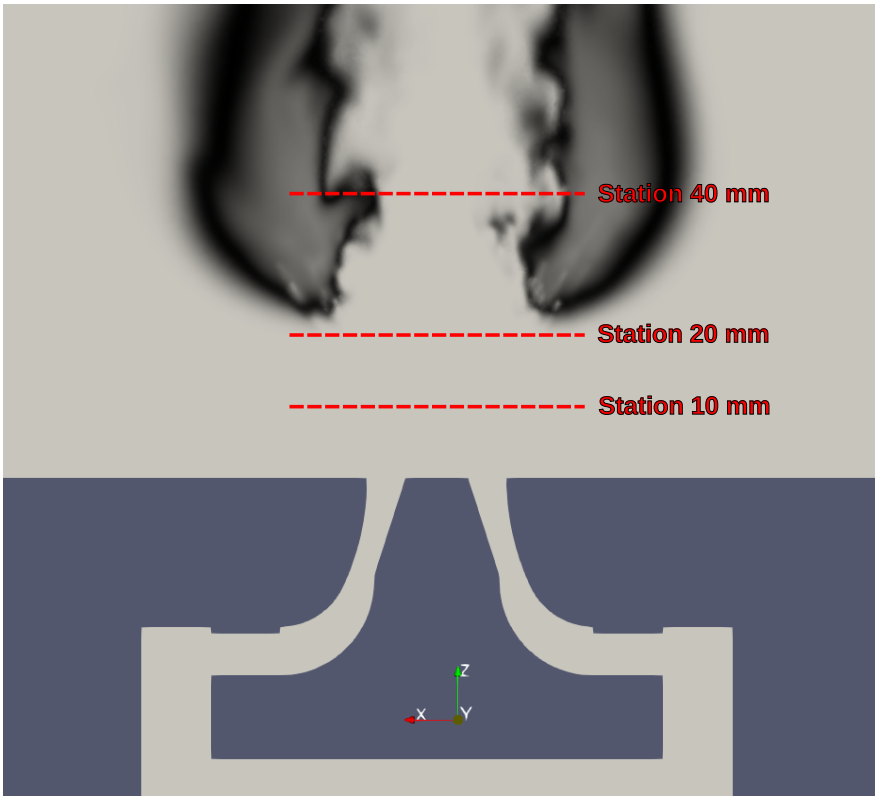

Figure 3: Sketch of the radial stations where LES results are compared with the experimental data. Stations are represented on a vertical central plane colored by temperature in order to visualize the position of the flame.

4.1. Flow field assessment

Firstly, the instantaneous and mean velocity magnitude in the vertical plane of the burner is shown in Fig. 4. The burner exhibits a flow pattern similar to that of an annular jet [26]. The air coming from the plenum enters the nozzle and accelerates, reaching the atmosphere with a velocity of 25 m/s, approximately. It is possible to appreciate a small recirculation zone near the position of the injector. In addition, the local increase of the velocity due to the droplet injection is visible, specially in the instantaneous contours of the left picture. Downstream, mixing decelerates the gas jet and it widens at an axial position of 25 mm due to

the presence of the flame, as it is shown in the contour plot of mean axial velocity (right side of Fig. 4).

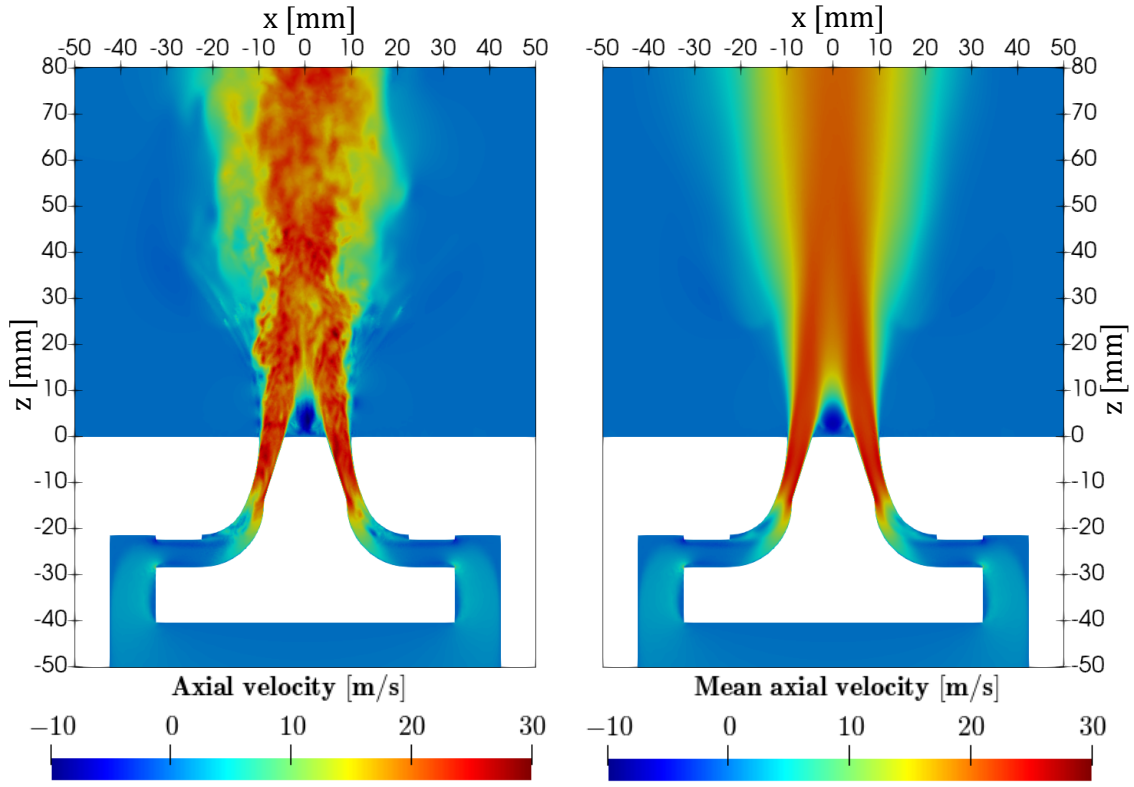

Figure 4: Fields of axial velocity on a vertical central plane. Left: instantaneous values, right: time-averaged values.

Fig. 5 shows the results obtained for the axial gas velocity. Mean and root mean square (RMS) values are compared with the experimental measurements at three different radial stations. Overall, the agreement between the simulation and the PDA measurements is satisfactory and ensure the correct aerodynamic stabilization of the flame. Results concerning the radial component of velocity are provided in Appendix.

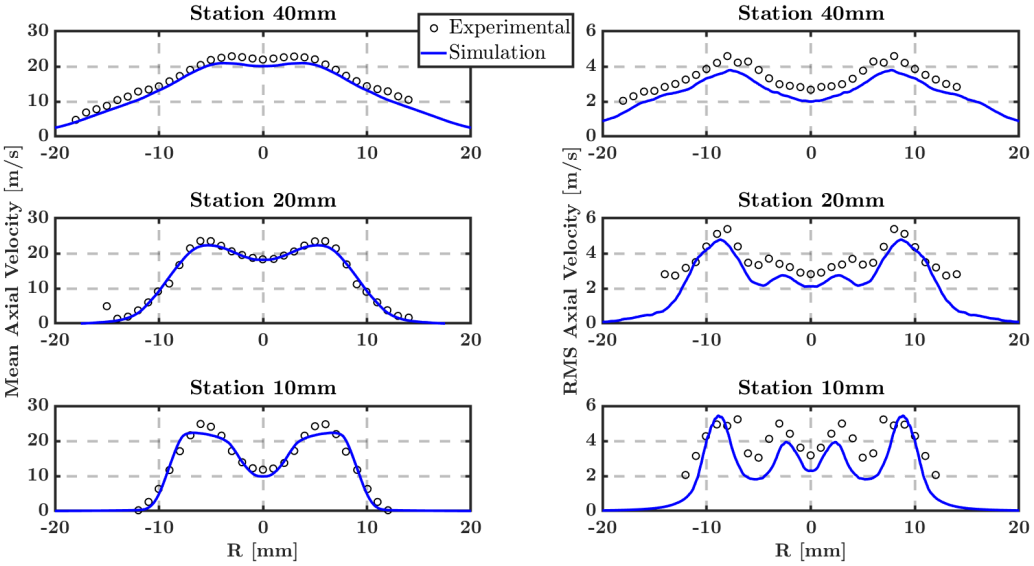

Figure 5: Comparison of axial velocity profiles at different radial stations for the gas phase. Left: mean values, right: RMS values. Blue lines: LES results, circles: experiments.

4.2. Dispersed phase

The results related to the dispersed phase are shown below. Fig. 6 shows an illustration of the spray in which droplets are colored by diameter (left) and axial velocity (right). As already described in previous works [38], this burner features the largest and inertial droplets at higher radial positions, as shown in Fig. 6 left. The largest droplet diameters are found matching the hollow-cone shape of the spray, while the smallest ones (with lower Stokes number) are located near the centerline. In terms of droplet velocity, it can be seen that these low inertial droplets, which follow the air stream coming from the annular nozzle, present a velocity closer to the gas phase at the axis. So that, in the right picture of Fig. 6, droplet axial velocity reaches values higher than 20 m/s in the central region, which is comparable with the values already seen in Fig. 5.

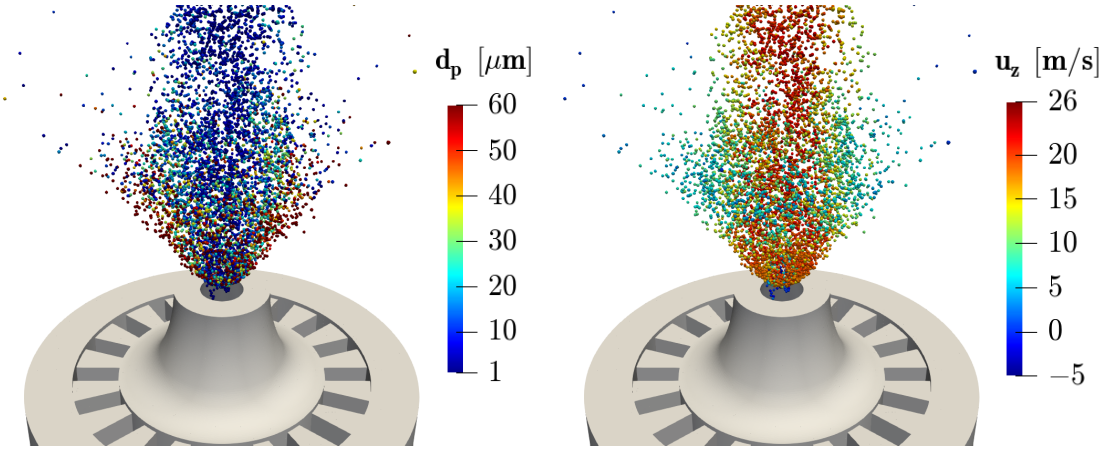

Figure 6: 3D view of the simulated hollow-cone spray. Left: spray colored by droplet diameter, right: spray colored by droplet axial velocity.

The droplet distribution according to their size can be seen in Fig. 7, where mean diameter is represented at different radial stations. In general, there is a good agreement between the simulation results and experiments.

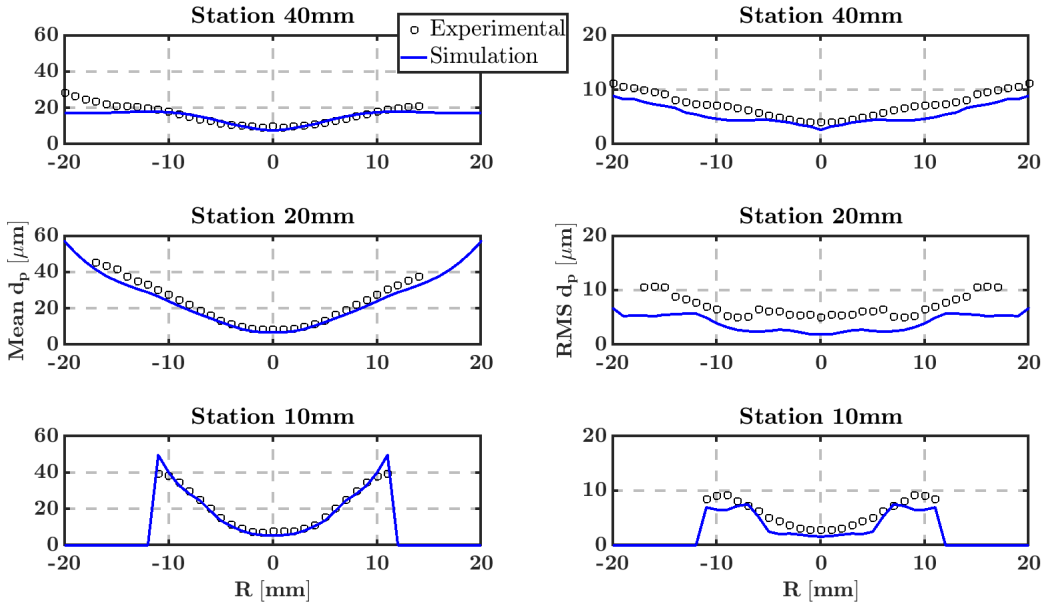

Figure 7: Comparison of droplet diameter profiles at different radial stations. Left: mean value, right: RMS value. Blue lines: LES results, circles: experiments.

Fig. 8 shows the comparison of axial droplet velocity (mean and RMS) with the measurements. Note that all droplets are considered to obtain reliable statistics of the liquid phase. Overall, there is good agree-

ment with the experimental data and the droplets statistics are well predicted. Due to the fact that the parameters of the spray model are adjusted to reproduce the experimental measurements at the nearest region, the simulation results at the station of 10 mm are well captured. In view of these results, it can be concluded the calibration of the fuel injection system is suitable for this case.

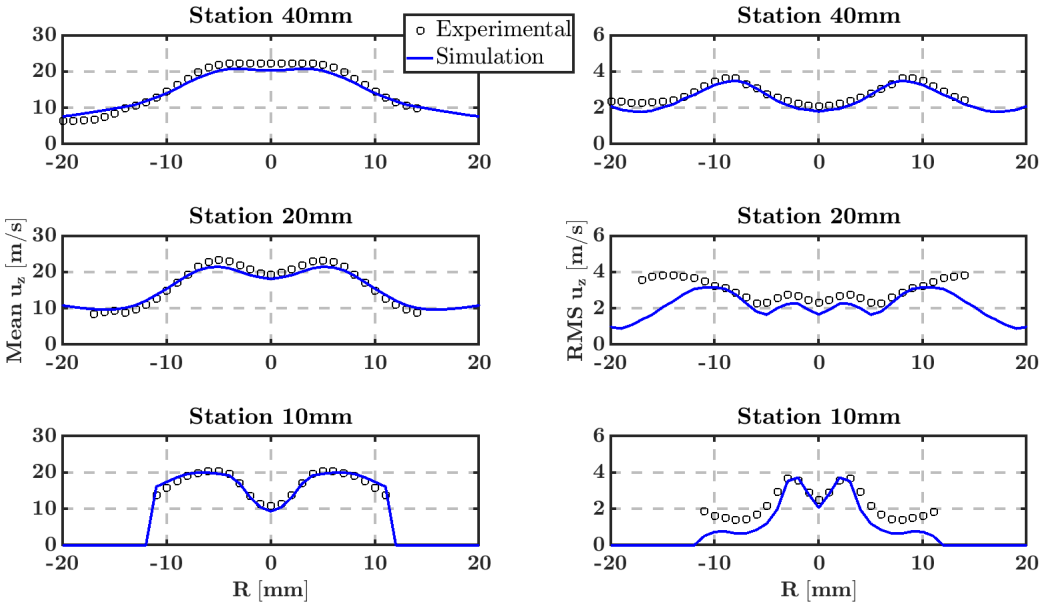

Figure 8: Comparison of droplet axial velocity profiles at different radial stations. Left: mean value, right: RMS value. Blue lines: LES results, circles: experiments.

4.3. Flame structure

In this section, results about the shape of the flame and its thermochemical structure are discussed. Figure 9 shows an instantaneous OH mass fraction contour, in which three regions can be clearly seen. Previous experimental studies have already identified the different areas of the flame [41, 42] and the same nomenclature will be followed in this work. The region of the flame closest to the injector, denoted as leading edge (LE) connects the two main reaction zones, namely the inner and outer reaction zones (IRZ and ORZ respectively). The ORZ exhibits a thick non-fluctuating OH layer and the IRZ presents a thinner and strongly wrinkled flame front, due to the turbulent air jet located close to the central axis of the burner. Regarding the combustion regime, the ORZ seems to be a quasi-steady diffusion flame, while the IRZ features a partially premixed flame propagation, as discussed by Shum-Kivan et al. [38].

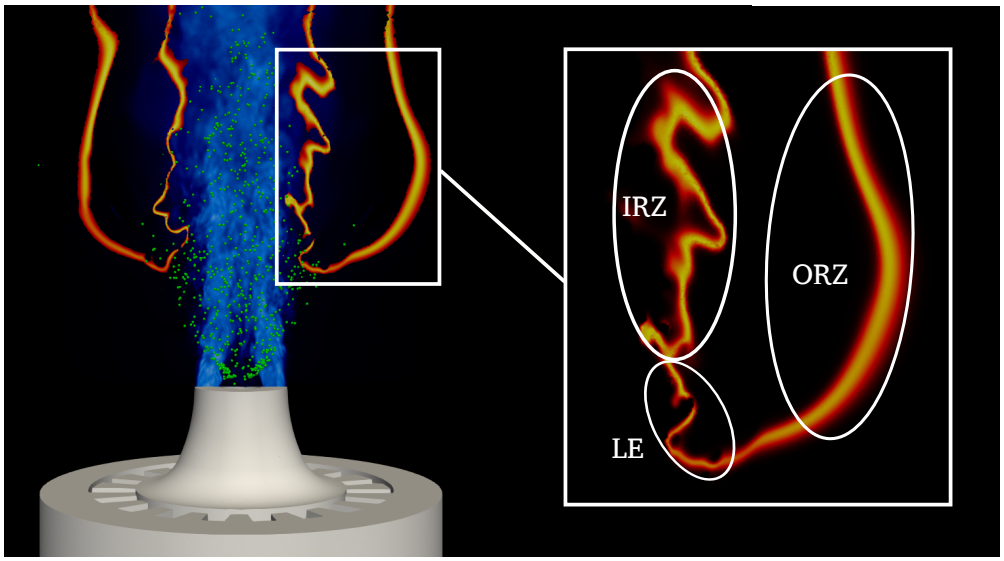

Figure 9: Different regions of the flame (LE, IRZ, ORZ) on a global view of the reaction front and flow field (red contours: OH concentration, blue contours: velocity magnitude, green: spray.

On the other hand, dynamics of the droplets and their interaction with the flame were also described in experimental and numerical works [38, 4, 39] and are revised here in light of the ability of unsteady flamelet approach to capture this interaction. Figure 9 shows droplets reaching the flame front at the LE, which correspond with the largest diameters due to the fact that they tend to follow the main spray direction, as previously discussed. Although there are many small droplets that follow the central air jet and evaporate in the region between the axis and the IRZ, most of the gaseous fuel comes from the evaporation of the large droplets crossing the reaction front and reaching the inside of the flame, due to the high temperature. Therefore, the maximum mixture fraction values are reached in the region between both IRZ and ORZ and closest to the LE, as shown in the first field of Fig. 10. Flow entrainment results in a reduction of the mixture fraction values further downstream. Furthermore, according to [42, 28], inside the flame and close to the ORZ the fuel thermal decomposition and incomplete combustion lead to the appearance of species such as CO, CO_2, H_2O and soot precursors (PAH). This phenomenon is well captured by the simulation, as it is observed in the mean fields of CO, CO_2 and C_2H_2 (which contributes to the formation of soot precursors [10]), presented in Fig. 10.

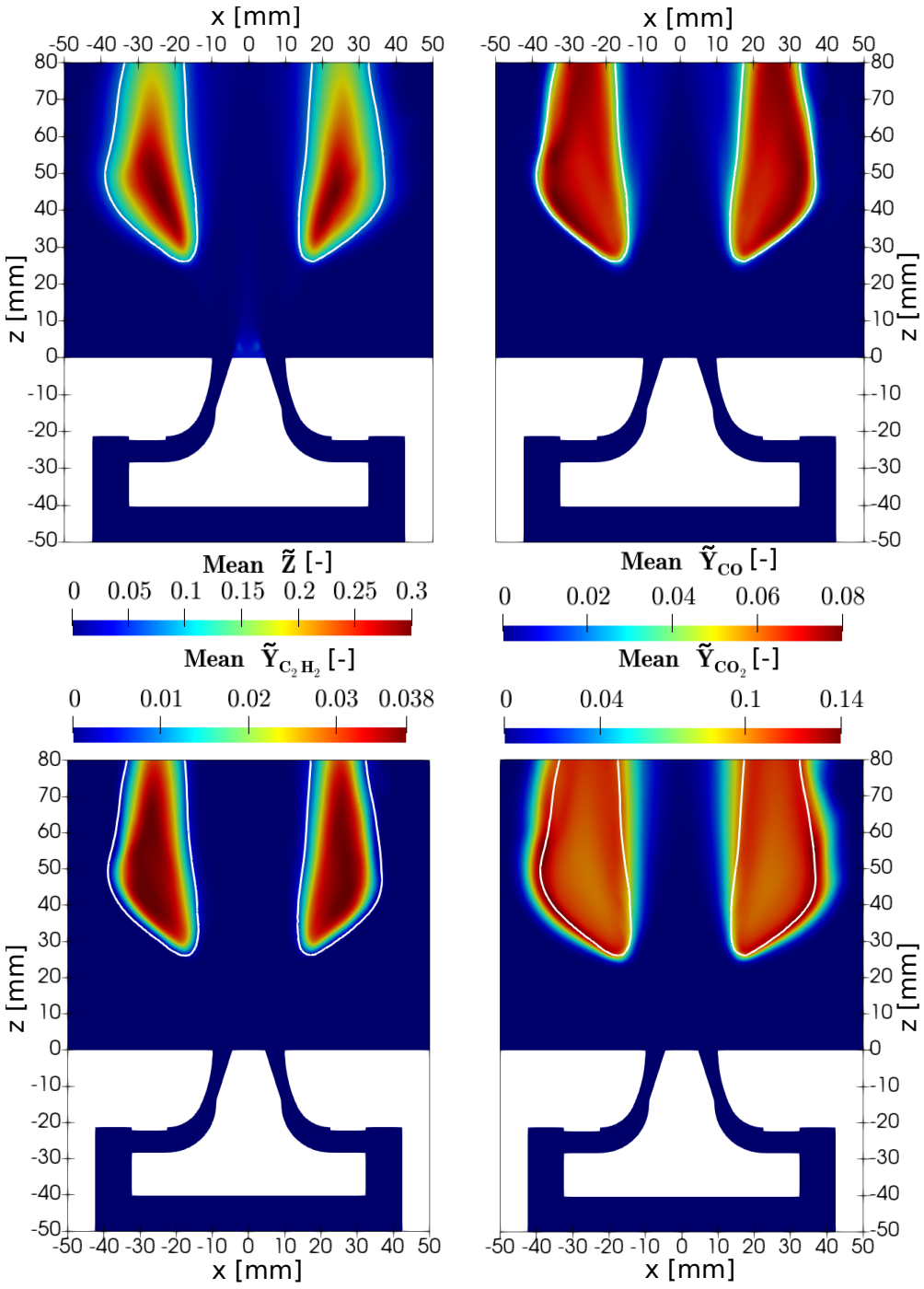

Figure 10: Mean contours of mixture fraction (top left), CO mass fraction (top right), C_2H_2 mass fraction (bottom left) and CO_2 mass fraction (bottom right). White line: mean stoichiometric mixture fraction iso-line.

A cut of the instantaneous stoichiometric mixture fraction iso-surface is observed in Fig. 11, together with the fuel spray colored by droplet diameter. This representation evidence the differences between the

regions of the flame described previously. In contrast with the uniform and homogeneous appearance of the ORZ, the IRZ presents small areas, near the leading edge of the flame, where the OH mass fraction decrease locally, while CH_2O mass fraction reach higher values. This particular behavior in the IRZ is related to the local extinction and re-ignition phenomena due not only to the droplets crossing the reaction front, but also to the interaction between the flame and the turbulent flow [42]. These aspects will be addressed in the next section.

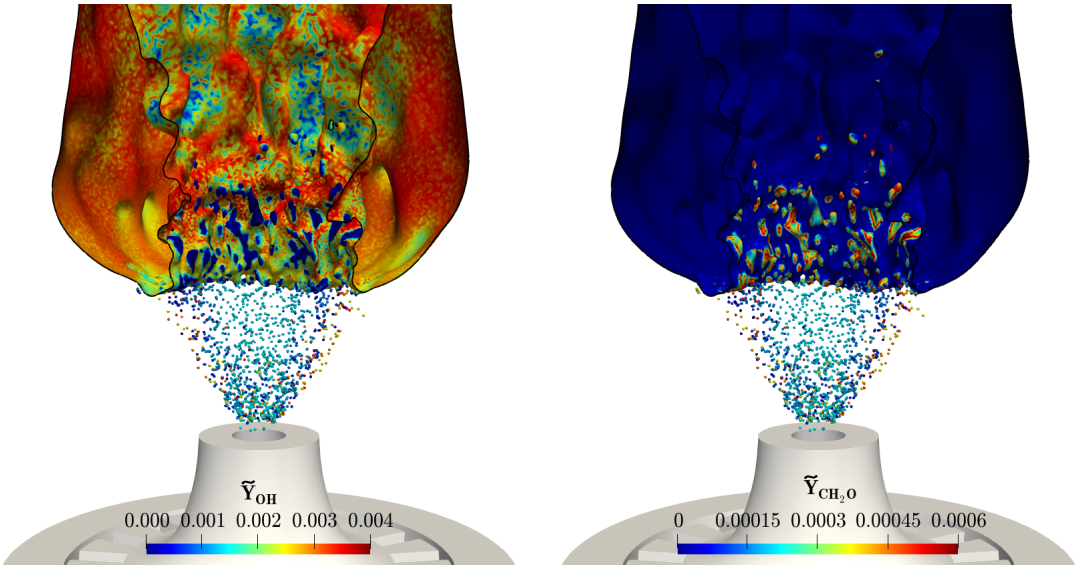

Figure 11: Vertical cut of the stoichiometric mixture fraction iso-surface colored by OH mass fraction (left), and CH_2O mass fraction (right). Spray droplets colored by diameter.

In order to perform a qualitative comparison of the flame topology, Fig. 12 shows mean and instantaneous OH contours from simulation and experimental measurement [42]. The overall shape of the flame can be observed to be well captured by the calculation. The positions of the IRZ and ORZ at $r \approx 13$ mm and $r \approx 35$ mm, respectively, are correctly predicted. Nevertheless, the shape of the outer flame is slightly different, with a wider radial distance between the IRZ and the ORZ for the calculations. It is important to note that discrepancies in the shape of the ORZ are consistent with those obtained in the radial velocity results for the gas phase at larger distances from the orifice (see Fig. 19). However, it is difficult to determine the reason for these differences, since experimental measurements are missing at this radial position and there is a large set of coupled factors affecting the ORZ.

The lift-off length is defined as the maximum value of progress variable gradient in the axial direction following a similar procedure to the experiments [29]. The time-averaged value of simulated lift-off length is approximately 25 mm, while the experimentally observed value is 25 ± 3 mm, so the proposed modelling

approach was able to predict the lift-off length on this flame quite accurately. Moreover, despite these simulations have reproduced some oscillations of the lift-off height, this aspect deserves further quantitative evaluation and it is left for future work.

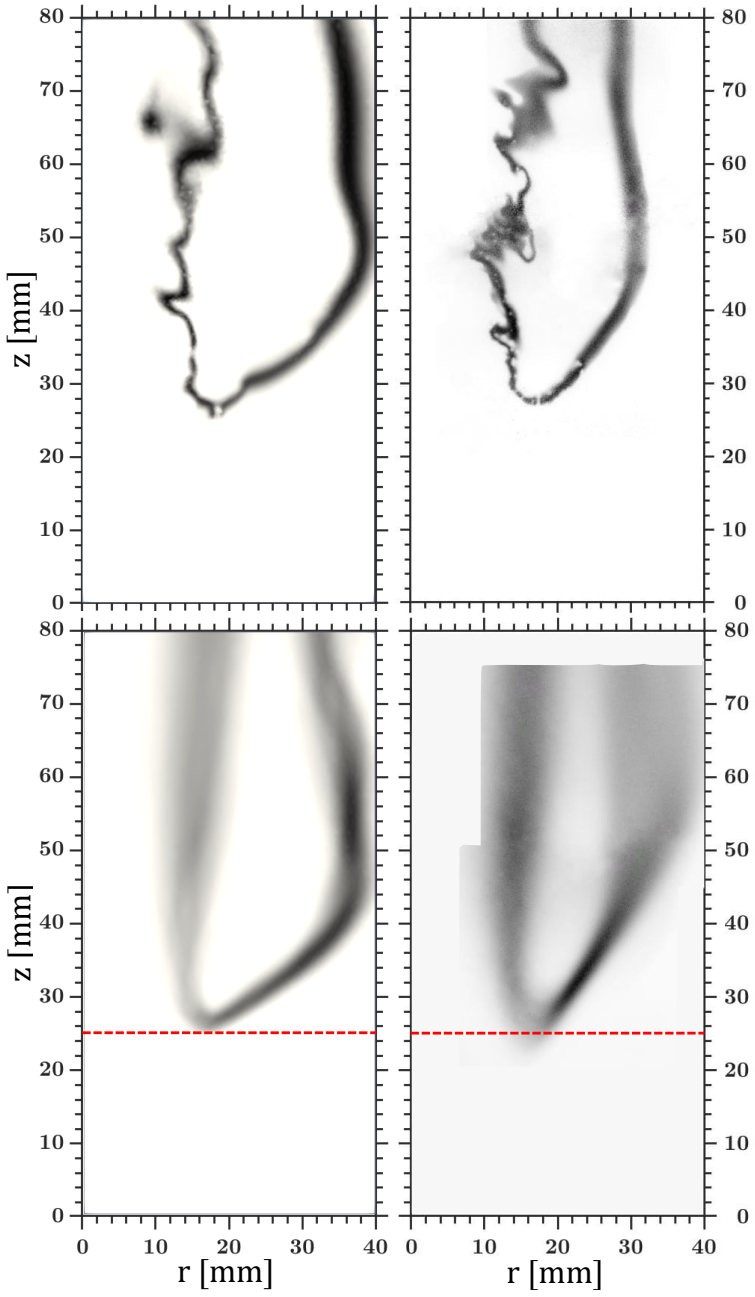

Figure 12: Comparison of OH contours. Left: LES results, right: OH-PLIF data from experiments [42]. Top: instantaneous signal, bottom: time-averaged fields. Red dashed line: mean lift-off length value.

4.4. Local extinction analysis

This section focuses on the analysis of the different mechanisms of extinction that appear in the inner layer of the flame and on the capability of the combustion model to predict them. According to the experimental studies [42], the flame exhibits localized extinction in the IRZ close to the leading edge (LE) and also downstream. Numerical simulations using LES will be used here to provide further understanding on this phenomena and shed some light in the principal mechanisms governing these effects.

4.4.1. Extinction due to droplet-flame interaction

Experimental observations [42] have shown the flame exhibits transient phenomena with some intermittency on the reacting layer, which is associated to existence of local extinction. Large droplets, which follow the main path of the spray, reach this region and impact the reacting layer causing rapid droplet evaporation and formation of rich pockets that quench the flame front. Figure 13 illustrates the extinction events at three different time instants. In the left column, contours of temperature and droplets are represented together, while the evaporation source term $\bar{S}_Z$ is shown on the right. In order to better visualize the position of the flame, a white iso-line representing the stoichiometric mixture fraction is included. An indicator of flame intermittency and localized extinction is the OH concentration, which is shown in Fig. 13 by a black line enclosing the regions with OH mass fraction $\widetilde{Y}_{OH}$ higher than 25% of peak values. The plots show a decrease in temperature close to the stoichiometric mixture fraction iso-line when the droplets cross the flame front, which is concurrent with a spatial intermittency in the OH signal. In fact, the contours of evaporation source term evidence high values of $\bar{S}_Z$ located near the extinction regions.

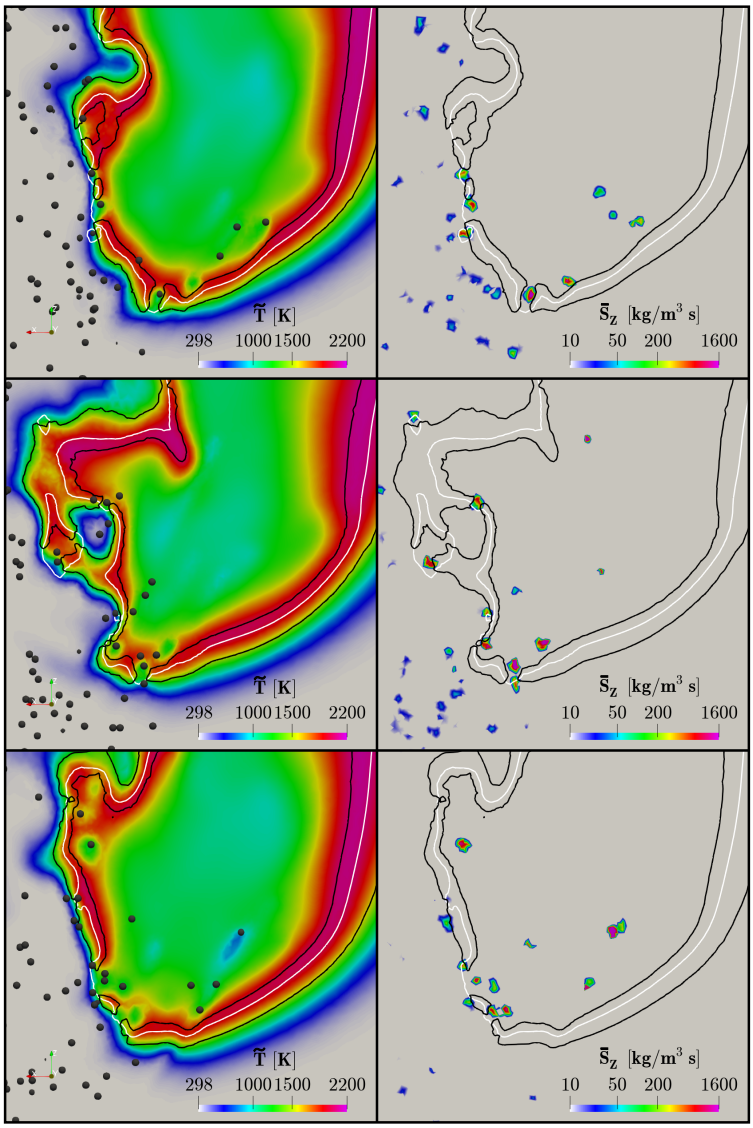

Figure 13: Extinction in the leading edge of the flame due to droplet interaction. Contours: temperature (left) and evaporation source term (right). Black line: threshold of 25% peak OH, white line: stoichiometric mixture fraction iso-line. Rows represent different time instants which are not equally time-spaced and illustrate clearly the phenomenon.

The analysis of the extinction by flame-droplet interactions is complemented with the results presented in Fig. 14. In this case, the figure shows a scatter plot of temperature and mixture fraction for different points located in the LE of the flame (points considered are located inside the LE region described in Fig. 9). The thermochemical variables are recorded within a 15 ms time window with a frequency of 0.05 ms, which correspond to 300 time samples. Points are colored by normalized progress variable $\widetilde{C}$, while solid and dashed lines represent the equilibrium values of the steady flamelets at adiabatic conditions ($\widetilde{i} = 1$) and at the highest heat loss ($\widetilde{i} = 0$), respectively. The blue line represents a steady adiabatic flamelet considering

non-zero mixture fraction variance (Z_v = 0.125). In this way, it is possible to evaluate quantitatively the phenomenon described in Fig. 13. Although temperature dispersion is clearly seen in a wide range of mixture fraction, the most interesting effect is observed near the stoichiometric conditions (vertical dotted line). The dispersion of temperature located in this region evidence that there are points very close to the reaction zone which experience extinction phenomena, showing a decrease in both temperature and normalized progress variable and moving away from chemical equilibrium conditions. Moreover, it is possible to appreciate that the peak in temperature values remains below the line of adiabatic conditions, closer to the maximum heat loss line. In this region, there are a large number of droplets crossing the flame front, evaporating and exchanging heat with the flame, which causes conditions of higher enthalpy losses. Points with higher values of mixture fraction that exceed the laminar adiabatic line are closer to the turbulent curve, since they are located inside the flame, where the mixture fraction variance Z_v reaches high values.

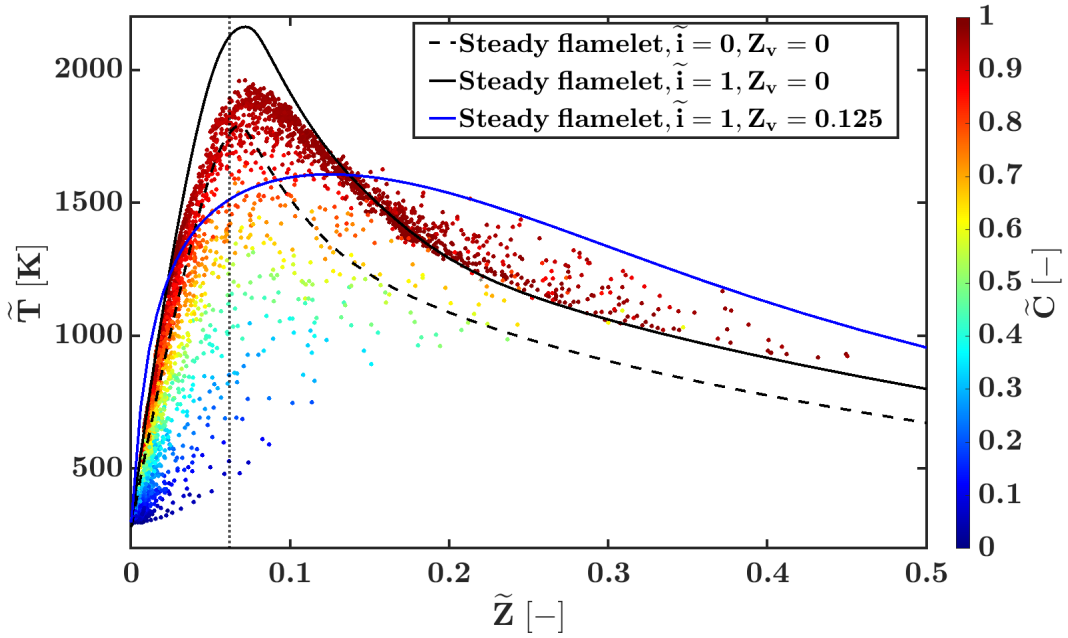

Figure 14: Scatter plot of temperature versus mixture fraction. Black dashed line: stoichiometric mixture fraction. Black solid lines: laminar steady flamelets. Blue solid line: turbulent steady flamelet. Colors: normalized progress variable.

In order to quantify the impact of droplet evaporation on the extinction process, Fig. 15 shows the correlation between the different magnitudes characterizing the extinction events. This includes normalized progress variable $\widetilde{C}$, OH mass fraction $\widetilde{Y}_{OH}$, formaldehyde mass fraction $\widetilde{Y}_{CH_2O}$ and evaporation source term $\bar{S}_Z$. Compared to Fig. 14, the mixture fraction of points located near the LE of the flame has been

conditioned in this case to a range of 20% around of the stoichiometric value and the evaporation mass rates are discretized in 30 bins. Each bin shows the averaged value of the magnitude and is colored by the standard deviation. Regarding the mixture fraction, the fuel/air concentration in this region fluctuates around the same mean (approximately the stoichiometric value) when the evaporation is low. As the evaporation rate increases, the formation of rich pockets contributes to increase locally the mixture fraction, while the reactivity of the mixture is reduced. Even for low evaporation rates, the normalized progress variable takes values $\widetilde{C} < 0.5$, and keeps reducing as $\bar{S}_Z$ increases. The same behavior is observed for the OH concentration. Due to this distribution of $\widetilde{Z}$ and $\widetilde{C}$, $\widetilde{Y}_{OH}$ is larger when the flame interacts with low concentrations of evaporated fuel. On the other hand, the concentration of CH_2O can be used as an indicator of the extinction events. The concentration of formaldehyde tends to behave opposite to OH, so CH_2O is close to zero with low evaporation rates and increases during extinction and re-ignition events. Furthermore, it is important to highlight that dispersion remains low for high values of $\bar{S}_Z$. When the evaporation rate reaches high values, extinctions are evident and $\widetilde{C}$ and $\widetilde{Y}_{OH}$ remain low or close to zero.

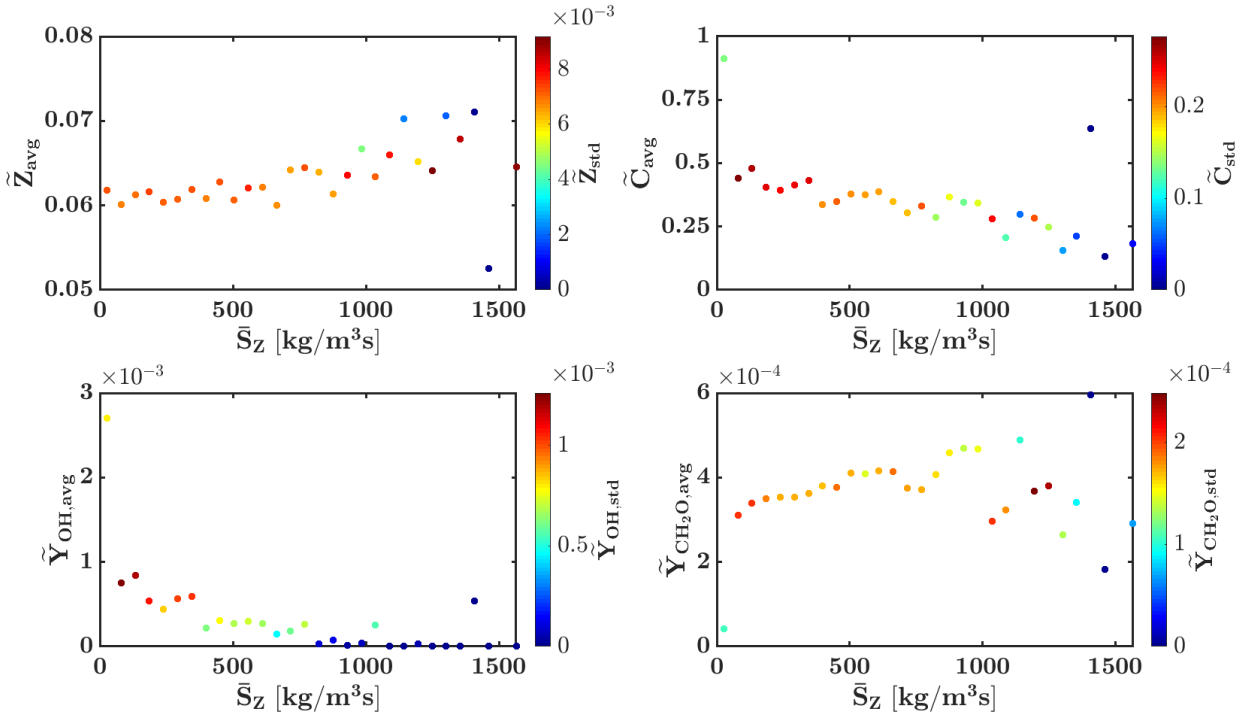

Figure 15: Correlation between droplet evaporation source term and mean mixture fraction (top left), normalized progress variable (top right), OH concentration (bottom left) and CH_2O concentration (bottom right). Colors: standard deviation of each magnitude.

4.4.2. Extinction due to turbulence-flame interactions

A second characteristic mechanism of flame front extinction is due to turbulence-flame interactions [42]. This phenomena occurs at axial positions further away from the LE of the flame, downstream in the IRZ, see Fig. 9. As described in the previous subsection, these events also exhibit the same features, that is low values of temperature, progress variable and OH concentration with high concentration of CH_2O. In this region, only small droplets that follow the main path of the gas jet evaporate close to the reacting layer and do not alter the flame front. As already described in the experimental work [42], the extinction of the flame in this region is associated to the stretching of the front produced by high levels of strain in the flow field. Figure 16 illustrates this event with a temporal sequence of the flame front obtained by LES. The strain is represented by a contour plot of the sum of resolved and subgrid scalar dissipation rates $\widetilde{\chi} = 2\tilde{D}\boldsymbol{\nabla}\tilde{Z}\cdot\boldsymbol{\nabla}\tilde{Z}+2\frac{Z_v}{\tau_{SGS}}$. Black and white iso-lines are associated with the OH threshold ($\widetilde{Y}_{OH} > 25\%$ of peak OH) and the stoichiometric mixture fraction, respectively. It can be clearly observed that when the scalar dissipation rate reaches high values near the reaction zone, the flame front becomes thinner and wrinkled until it eventually quenches. This is a slower event than the extinction located at the LE of the flame, where the appearance of high evaporation rates close to the flame front produces its extinction very rapidly. In this case, quenching occurs when the front is affected by high scalar dissipation rate values during certain time. Note that the time window of this temporal sequence corresponds to 1 ms, which is sufficient to find an extinction event associated with strain, since the time scale of this phenomenon is approximately 0.7 ms, as introduced in Section 2. The current LES is able to reproduce these extinction events and evidence the same quenching features as those observed in the experimental measurements [42].

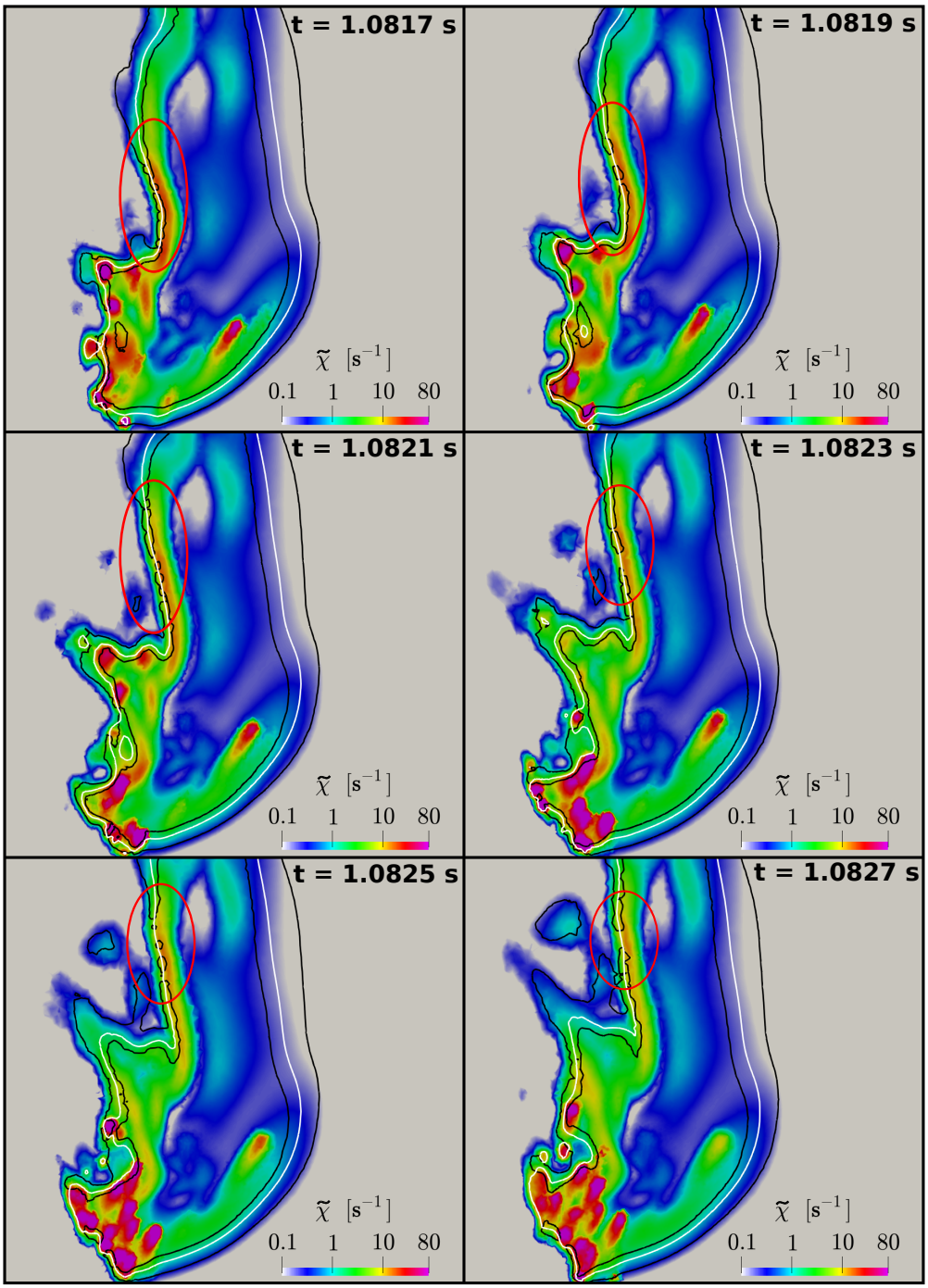

Figure 16: Temporal sequence of an extinction event due to strain, where each row represents a different time instant with a time separation of 0.2 ms. Contours: scalar dissipation rate. Black line: threshold of 25% peak OH, white line: stoichiometric mixture fraction iso-line.

In the same way as in the previous section, the analysis is complemented with some scatter plots in order to quantify the extinction phenomenon. Fig. 17 shows both $\widetilde{T} - \widetilde{Z}$ and $\widetilde{T} - \widetilde{\chi}$ scattered data for points

located in the IRZ (the region affected by extinction due to turbulence-flame interactions). The methodology followed is similar to that of Fig. 14. Regarding the $\widetilde{T} - \widetilde{Z}$ plot (left side), the dispersion of temperature for mixture fraction values ranged between 0 and 0.2 is also evident in this region of the IRZ. Considering the points near the stoichiometric conditions allows to clearly observe the decrease of both temperature and progress variable, as a result of the quenching events. Besides, the temperature peak located at slightly rich mixtures is closer to the adiabatic conditions, compared to the LE region of the flame, see Fig. 14. As mentioned above, the evaporation rate is considerably lower in this region, therefore enthalpy losses due to heat transfer between the flame and droplets are also lower. On the other hand, the plot on the right side of Fig. 17 shows the scattered data of temperature related to the scalar dissipation rate for points located at the stoichiometric mixture fraction iso-surface within the IRZ. For low values of $\widetilde{\chi}$ ($\widetilde{\chi} < 1$ [s^{-1}]), all points are present in the region of high temperature, which represent the stable flame conditions. Temperature dispersion appears when $\widetilde{\chi} > 1$ [s^{-1}], showing extinction and re-ignition events in a wide range of $\widetilde{\chi}$ values. Note that extinction events appear for $\widetilde{\chi}$ values lower than the quenching scalar dissipation rate for laminar adiabatic steady flamelet ($\chi_{ext,lam} \approx 80$ [s^{-1}], see Fig. 1b). Thus, it is not necessary to reach this condition in order to find an extinction event, which has already been observed in other turbulent flames and modelling approaches [11, 44].

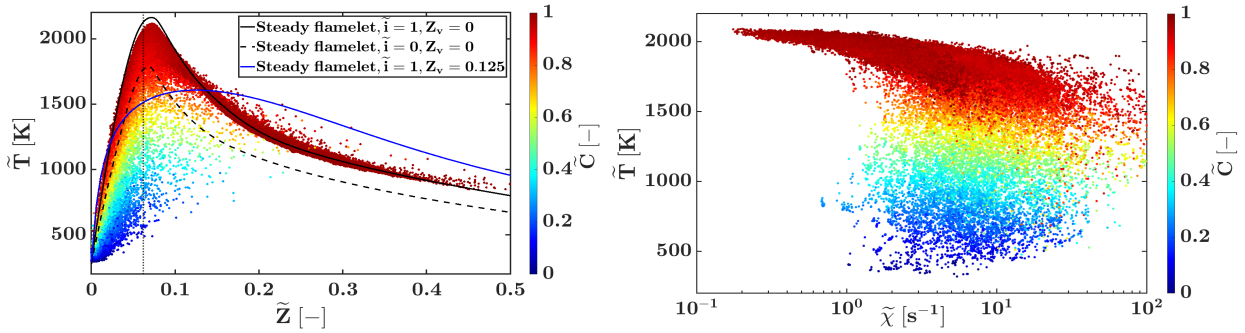

Figure 17: Scattered data of temperature versus mixture fraction in the IRZ (left) and of temperature versus scalar dissipation rate for points on the stoichiometric mixture fraction iso-surface (right). Vertical black dashed line: stoichiometric mixture fraction. Black solid lines: laminar steady flamelets. Blue solid line: turbulent steady flamelet. Colors: normalized progress variable.

The same information for OH and CH_2O mass concentration is presented in Fig. 18. In this case, points coloured by the normalized progress variable correspond to all the data of the stoichiometric surface within the region of the IRZ affected by strain. The scatter data is recorded during 10 ms, while black squares and error bars indicate the mean value and the standard deviation, respectively. Due to the fact that there are many points of the flame front burning stable even for high values of $\widetilde{\chi}$, mean $\widetilde{Y}_{OH}$ decreases more slowly

with $\widetilde{\chi}$, compared to those of the region affected by droplet evaporation (Fig. 15). However, it is important to highlight the level of fluctuations of OH and CH_2O concentrations. The remarkable increase in the fluctuations of these magnitudes with the scalar dissipation rate shows that extinctions generally occur for high $\widetilde{\chi}$ values, in a similar range to that observed for the dispersion of temperature in Fig. 17. In addition, the inverse relation between $\widetilde{Y}_{OH}$ and $\widetilde{Y}_{CH_2O}$ can be distinguished again [11], and suggests that formaldehyde can be used as an indicator to predict unsteady combustion phenomena like localized extinction.

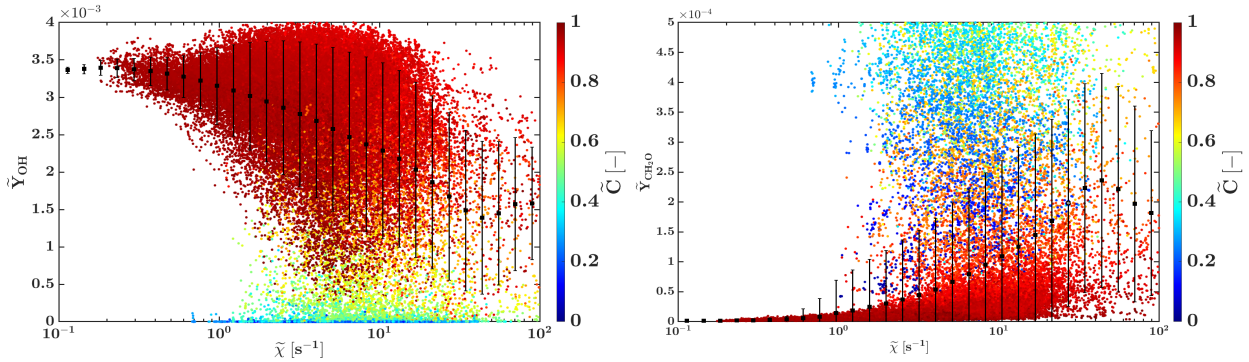

Figure 18: Effect of the scalar dissipation rate on OH (left) and CH_2O (right) concentrations. Data collected on the stoichiometric mixture fraction iso-surface between $z = 35$ *mm* and $z = 60$ *mm* (region extinguished due to strain). Black squares: mean value, errorbars: standard deviation. Colors: normalized progress variable.

5. Conclusions

In this work, large eddy simulations of the CRSB n-heptane spray flame have been performed using a Eulerian-Lagrangian description of the two-phase flow. A Lagrangian Particle Tracking approach has been used to evaluate the characteristics of the dispersed phase with two-way coupling with the carrier phase. A modelling approach based on the tabulation of steady and unsteady extinguishing diffusion flamelets at different enthalpy levels together with a presumed shape PDF has been employed as turbulent combustion model.

An assessment of the predictions of the liquid phase and flow characteristics have been conducted and good agreement with the experimental measurements was achieved for droplet and gas velocities and fluctuations. The numerical results were able to predict the flame topology and identify the different regions of the flame. In particular, the numerical results successfully predicted the flame lift-off-length and the wrinkled shape and position of the inner flame.

In addition to the validation part, the work is focused on the study and characterization of the extinction phenomena occurring in different regions of the spray flame. The flame exhibits localized extinction in the

inner reaction zone close to the leading edge due to the interaction of the droplets with the flame front, while extinction events also occur further downstream in the inner region due to the high turbulence level.

Close to the injector and near the leading edge, the simulations show a strong interaction between droplets and the flame front, which is also confirmed by the experimental results. The flame front shows some intermittency on the OH concentration with the presence of high values of CH_2O indicating the existence of localized extinction. The analysis of the evaporation source term evidences the relationship between the formation of fuel rich pockets and the quenching process. Calculation results show a decrease in temperature close to the stoichiometric mixture fraction contours when the droplets cross the flame front, coinciding with a spatial intermittency in the OH signal, which correspond to locations of high evaporation rates.

A similar behaviour is found downstream in the inner region of the flame. In this case, the extinction of the flame is associated to the stretching of the reacting front produced by high levels of turbulence in the flow field. In this study, this interaction has been quantified in terms of the scalar dissipation rate along with OH and CH_2O concentrations. It was shown that when the scalar dissipation rate reaches high values near the reaction zone, the flame front becomes thinner and wrinkled until it eventually quenches. Quenching was shown to occur when the front is affected by high scalar dissipation rates during certain time. This process is characterized by larger time-scales than the extinction by droplet-flame interactions.

The similarity of the resulting OH and CH_2O concentration during the two types of extinction events suggests that CH_2O can be used as an indicator to predict unsteady combustion phenomena such as localized extinction. Finally, it can be concluded that the proposed modelling framework in LES was able to reproduce the transient extinction events in the inner reaction zone of the flame and can be used to investigated flame extinction and re-ignition in combustion problems.

Acknowledgments

This work was partially funded by the Spanish Ministerio de Economía y Competitividad within the frame of the CHEST (TRA2017-89139-C2-1-R) project. BSC also acknowledges the funding from the CoEC project through the European Union's Horizon 2020 research and innovation programme under grant agreement No 952181. Authors acknowledge the computer resources at Marenostrum and the technical support provided by Barcelona Supercomputing Center (BSC) (IM-2019-3-0025, IM-2020-1-0017, IM-2020-2-0026). Authors also thank the access to the CRSB database kindly provided by Prof. B. Renou.

Appendix

Some additional figures regarding the gas and liquid phase assessment are provided in this appendix. In the following figures, the comparison between simulation and experiments of radial gas phase (Fig. 19) and droplet (Fig. 20) velocity is shown.

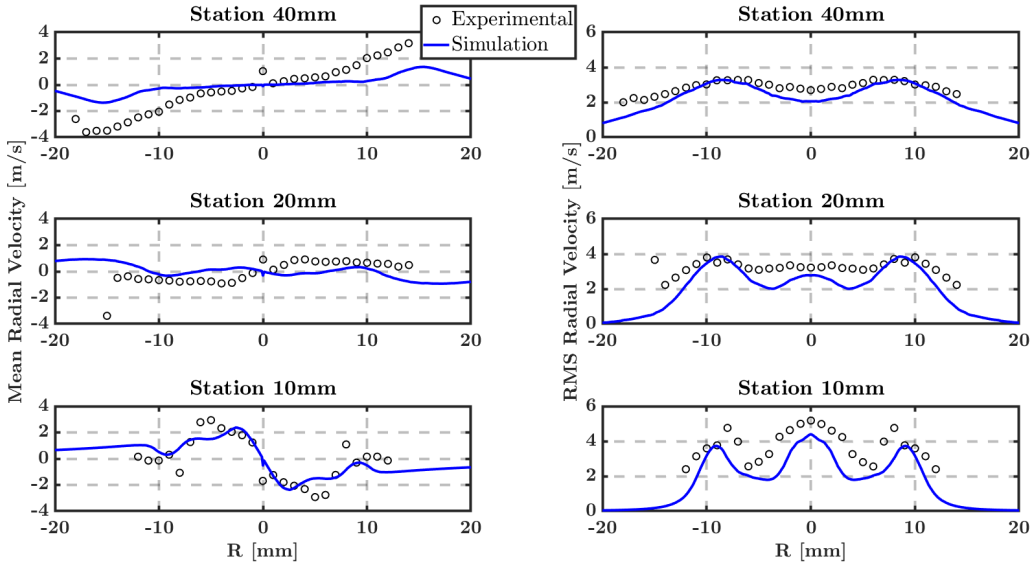

Figure 19: Comparison of radial velocity profiles at different radial stations for the gas phase. Left: mean values, right: RMS values. Blue lines: LES results, circles: experiments.

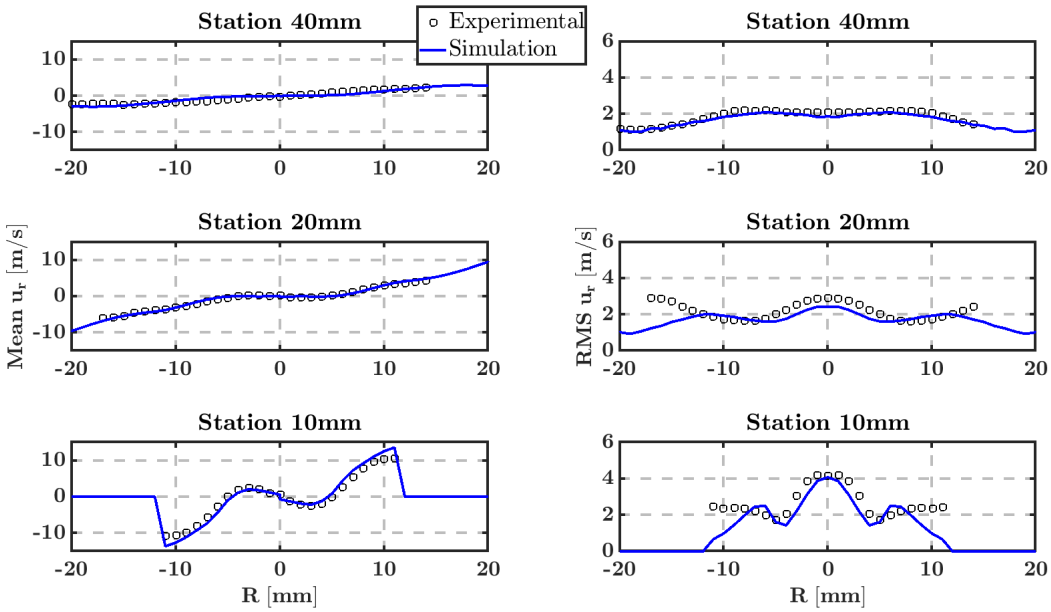

Figure 20: Comparison of droplet radial velocity profiles at different radial stations. Left: mean value, right: RMS value. Blue lines: LES results, circles: experiments.

References

[1] B Abramzon and W A Sirignano. "Droplet vaporization model for spray combustion calculations". In: *International journal of heat and mass transfer* 32.9 (1989), pp. 1605–1618.

[2] A. Both. "RANS-FGM simulation of n-heptane spray flame in OpenFOAM". MA thesis. Delft University of Technology, 2017.

[3] Ambrus Both et al. "Low-dissipation finite element strategy for low Mach number reacting flows". In: *Computers & Fluids* 200 (2020), p. 104436.

[4] Adrien Chatelier et al. "Large Eddy Simulation of a Turbulent Spray Jet Flame Using Filtered Tabulated Chemistry". In: *Journal of Combustion* 2020 (2020). ISSN: 20901976. DOI: 10.1155/2020/2764523.

[5] CHEM1D. *A one dimensional flame code. Eindhoven University of Technology*. 2002.

[6] S. Delhaye et al. "Incorporating unsteady flow-effects beyond the extinction limit in flamelet-generated manifolds". In: *Proceedings of the Combustion Institute* 32.1 (2009), pp. 1051–1058. ISSN: 1540-7489. DOI: https://doi.org/10.1016/j.proci.2008.06.111.

[7] P. Domingo, L. Vervisch, and D. Veynante. "Large-eddy simulation of a lifted methane jet flame in a vitiated coflow". In: *Combustion and Flame* 152.3 (2008), pp. 415–432. ISSN: 0010-2180. DOI: http://dx.doi.org/10.1016/j.combustflame.2007.09.002.

[8] Frederick L. Dryer. "Chemical kinetic and combustion characteristics of transportation fuels". In: *Proceedings of the Combustion Institute* 35.1 (2015), pp. 117–144. ISSN: 1540-7489. DOI: https://doi.org/10.1016/j.proci.2014.09.008.

[9] Benoit Fiorina et al. "Modelling non-adiabatic partially premixed flames using flame-prolongation of ILDM". In: *Combustion Theory and Modelling* 7.3 (2003), p. 449.

[10] Michael Frenklach et al. "Detailed kinetic modeling of soot formation in shock-tube pyrolysis of acetylene". In: *Symposium (International) on Combustion* 20.1 (1985). Twentieth Symposium (International) on Combustion, pp. 887–901. ISSN: 0082-0784. DOI: https://doi.org/10.1016/S0082-0784(85)80578-6.

[11] A. Giusti and E. Mastorakos. "Detailed chemistry LES/CMC simulation of a swirling ethanol spray flame approaching blow-off". In: *Proceedings of the Combustion Institute* 36.2 (2017), pp. 2625–2632. ISSN: 15407489. DOI: 10.1016/j.proci.2016.06.035.

[12] A. Giusti and E. Mastorakos. "Turbulent Combustion Modelling and Experiments: Recent Trends and Developments". In: *Flow, Turbulence and Combustion* 103 (2019), pp. 1–18.

[13] Guillaume Houzeaux et al. "Dynamic load balance applied to particle transport in fluids". In: *International Journal of Computational Fluid Dynamics* 30.6 (2016), pp. 408–418.

[14] Matthias Ihme and Heinz Pitsch. "Prediction of extinction and reignition in nonpremixed turbulent flames using a flamelet/progress variable model. 2. Application in LES of Sandia flames D and E". In: *Combustion and Flame* 155.1-2 (2008), pp. 90–107. DOI: 10.1016/j.combustflame.2008.04.015.

[15] Enric Illana, Daniel Mira, and Arnaud Mura. "An extended flame index partitioning for partially premixed combustion". In: *Combustion Theory and Modelling* 25.1 (2021), pp. 121–157. DOI: 10.1080/13647830.2020.1841912.

[16] Patrick Jenny, Dirk Roekaerts, and Nijso Beishuizen. "Modeling of turbulent dilute spray combustion". In: *Progress in Energy and Combustion Science* 38.6 (2012), pp. 846–887. DOI: 10.1016/j.pecs.2012.07.001.

[17] Weiqi Ji et al. "Dependence of kinetic sensitivity direction in premixed flames". In: *Combustion and Flame* 220 (2020), pp. 16–22. ISSN: 0010-2180. DOI: https://doi.org/10.1016/j.combustflame.2020.06.027.

[18] William P. Jones, Andrew J. Marquis, and Dongwon Noh. "An investigation of a turbulent spray flame using Large Eddy Simulation with a stochastic breakup model". In: *Combustion and Flame* 186 (2017), pp. 277–298. ISSN: 15562921. DOI: 10.1016/j.combustflame.2017.08.019.

[19] Amable Liñán et al. "The large-activation-energy analysis of extinction of counterflow diffusion flames with non-unity Lewis numbers of the fuel". In: *Combustion and Flame* 175 (2017), pp. 91–106. ISSN: 0010-2180. DOI: https://doi.org/10.1016/j.combustflame.2016.06.030.

[20] Tianfeng Lu and Chung K Law. "Linear time reduction of large kinetic mechanisms with directed relation graph: n-Heptane and iso-octane". In: *Combustion and Flame* 144.1 (2006), pp. 24–36. DOI: https://doi.org/10.1016/j.combustflame.2005.02.015.

[21] Likun Ma. "Computational modeling of turbulent spray combustion". PhD thesis. Delft University of Technology, 2016.

[22] Likun Ma and Dirk Roekaerts. "Modeling of spray jet flame under MILD condition with non-adiabatic FGM and a new conditional droplet injection model". In: *Combustion and Flame* 165 (2016), pp. 402–423. ISSN: 15562921. DOI: 10.1016/j.combustflame.2015.12.025.

[23] Likun Ma and Dirk Roekaerts. "Numerical study of the multi-flame structure in spray combustion". In: *Proceedings of the Combustion Institute* 36 (2017), pp. 2603–2613. ISSN: 15407489. DOI: 10.1016/j.proci.2016.06.015.

[24] 7th Workshop on Measurement and Computation of Turbulent Spray Combustion (TCS7). In: (2019). URL: http://www.tcs-workshop.org/.

[25] D Mira et al. "Numerical characterization of a premixed hydrogen flame under conditions close to flashback". In: *Flow, Turbulence and Combustion* 104.2 (2020), pp. 479–507.

[26] D. Mira and X. Jiang. "Large-eddy simulations of unsteady hydrogen annular flames". In: *Computers & Fluids* 80 (2013). Selected contributions of the 23rd International Conference on Parallel Fluid Dynamics ParCFD2011, pp. 429–440. ISSN: 0045-7930. DOI: https://doi.org/10.1016/j.compfluid.2012.01.013.

[27] D. Mira et al. "Numerical assessment of subgrid scale models for scalar transport in large-eddy simulations of hydrogen-enriched fuels". In: *International Journal of Hydrogen Energy* 39.14 (2014), pp. 7173–7189. ISSN: 0360-3199. DOI: https://doi.org/10.1016/j.ijhydene.2014.03.018.

[28] Irfan A. Mulla and Bruno Renou. "Simultaneous imaging of soot volume fraction, PAH, and OH in a turbulent n-heptane spray flame". In: *Combustion and Flame* (2019). ISSN: 15562921. DOI: 10.1016/j.combustflame.2019.08.012.

[29] Irfan A. Mulla et al. "Quantitative imaging of nitric oxide concentration in a turbulent n-heptane spray flame". In: *Combustion and Flame* 203 (2019), pp. 217–229. ISSN: 15562921. DOI: 10.1016/j.combustflame.2019.02.005.

[30] Dongwon Noh et al. "Comparison of droplet evaporation models for a turbulent, non-swirling jet flame with a polydisperse droplet distribution". In: *Combustion and Flame* 194 (2018). ISSN: 15562921. DOI: 10.1016/j.combustflame.2018.04.018.

[31] J.A. Van Oijen and L.P.H. De Goey. "Modelling of Premixed Laminar Flames using Flamelet-Generated Manifolds". In: *Combustion Science and Technology* 161.1 (2000), pp. 113–137. DOI: 10.1080/00102200008935814.

[32] N. Peters. "Laminar diffusion flamelet models in non-premixed turbulent combustion". In: *Progress in Energy and Combustion Science* 10.3 (1984), pp. 319–339. ISSN: 0360-1285. DOI: https://doi.org/10.1016/0360-1285(84)90114-X.

[33] Charles D. Pierce and Parviz Moin. "Progress-variable approach for large-eddy simulation of non-premixed turbulent combustion". In: *Journal of Fluid Mechanics* 504.504 (2004), pp. 73–97. ISSN: 00221120. DOI: 10.1017/S0022112004008213.

[34] Heinz Pitsch, Chong M. Cha, and Sergei Fedotov. "Flamelet modelling of non-premixed turbulent combustion with local extinction and re-ignition". In: *Combustion Theory and Modelling* 7.2 (June 2003), pp. 317–332. DOI: 10.1088/1364-7830/7/2/306.

[35] Thierry Poinsot and Denis Veynante. *Theoretical and numerical combustion*. RT Edwards, Inc., 2005.

[36] S.B. Pope. "Ten questions concerning the large-eddy simulation of turbulent flows". In: *New Journal of Physics* 6 (2004). ISSN: 13672630. DOI: 10.1088/1367-2630/6/1/035.

[37] W E Ranz and W R Marshall. "Evaporation from drops: Part 1". In: *Chem. eng. prog* 48.3 (1952), pp. 141–146.

[38] F. Shum-Kivan et al. "Experimental and numerical analysis of a turbulent spray flame structure". In: *Proceedings of the Combustion Institute* 2 (2017), pp. 2567–2575. ISSN: 15407489. DOI: 10.1016/j.proci.2016.06.039.

[39] Michael Philip Sitte and Epaminondas Mastorakos. "Large Eddy Simulation of a spray jet flame using Doubly Conditional Moment Closure". In: *Combustion and Flame* 199 (2019), pp. 309–323. DOI: 10.1016/J.COMBUSTFLAME.2018.08.026.

[40] M. Vazquez et al. "Multiphysics engineering simulation toward exascale". In: *J. Comput. Sci.* 14 (2016), pp. 15–27.

[41] Antoine Verdier et al. "Experimental study of local flame structures and fuel droplet properties of a spray jet flame". In: *Proceedings of the Combustion Institute* 36.2 (2017), pp. 2595–2602. ISSN: 15407489. DOI: 10.1016/j.proci.2016.07.016.

[42] Antoine Verdier et al. "Local extinction mechanisms analysis of spray jet flame using high speed diagnostics". In: *Combustion and Flame* 193 (2018), pp. 440–452. ISSN: 15562921. DOI: 10.1016/j.combustflame.2018.03.032.

[43] AW Vreman. "An eddy-viscosity subgrid-scale model for turbulent shear flow: Algebraic theory and applications". In: *Physics of fluids* 16.10 (2004), pp. 3670–3681.

[44] S. Yu et al. "LES/PDF modeling of swirl-stabilized non-premixed methane/air flames with local extinction and re-ignition". In: *Combustion and Flame* 219 (2020), pp. 102–119. ISSN: 15562921. DOI: 10.1016/j.combustflame.2020.05.018.

[45] M. C. Yuen and L. W. Chen. "On drag of evaporating liquid droplets". In: *Combustion Science and Technology* 14.4-6 (1976), pp. 147–154. DOI: 10.1080/00102207608547524.